



COLUMBIA | ENGINEERING
The Fu Foundation School of Engineering and Applied Science

SENIOR DESIGN '20

EXP



Due to COVID-19 and the transition to a virtual learning environment, Senior Design projects were not able to be completed to the standard of previous years. This booklet consists of projects that were voluntarily submitted to be showcased.

Table of Contents

Applied Physics and Applied Mathematics	3
Biomedical Engineering	5
Civil Engineering and Engineering Mechanics	12
Chemical Engineering	14
Electrical Engineering	16
Mechanical Engineering	48

APPLIED PHYSICS AND APPLIED MATHEMATICS

To view all projects, please visit: <https://apam.columbia.edu/2020-mse-senior-design-project>

Developing a Simple and Universal Method to Manufacture High Performance Radiative Cooling Fabrics

Chixuan Chen

Advisor: Professor Yuan Yang, Department of Applied Physics and Applied Mathematics

Paper and Copper Pigment Degradation in European Early Printed Books

Natasha Mohan

Advisor: Professor Katy Barmak, Department of Applied Physics and Applied Mathematics

Effect of Nb Doping on Performance of Cathodes

Mateo Navarro Goldaraz

Advisor: Professor Lauren Marbella, Department of Chemical Engineering

Selective Amorphization of Thin Film Metals with ELA for Corrosion Protection in MEMS Production

William Randolph

Advisor: Professor James Im, Department of Applied Physics and Applied Mathematics

Mechanical Characterization of Ash-Based Lightweight Geopolymer Aggregate

Nicholas Vallin

Advisor: Professor Shiho Kawashima, Department of Civil Engineering

Layer-by-Layer Deposition to Synthesize Stretchable Gas Barrier

Miguel Yepes

Advisor: Professor Xi Chen, Department of Earth and Environmental Engineering

BIOMEDICAL ENGINEERING

Gash Guardian

Sofia Barbosa, Brailey Faris, Kelsey Gray, Kevin Park, Anya Volter

Advisors: Prof. Clark Hung

58% of Americans experience or know someone who has experienced gun violence. Exsanguination for the average adult happens within four minutes of injury, leading to 56% of gun-related fatalities occurring before a victim reaches a hospital. This is largely attributable to untrained bystanders' inability to stop bleeding. There are effective solutions to treat gunshot wounds, but they rely on pre-existing expertise or physical abilities. In case of a shooting, civilians need an easy-to-use device to mitigate blood loss until emergency medical care arrives.

We have created a user-friendly device that mitigates blood loss by creating an encapsulating seal around a wound. A silicon-plastic cup loaded with a coagulating material covers the wound and a seal is created around the wound, forming a space to restrict blood loss. The silicone attachment conforms to body curvature, making the device applicable to a variety of body locations. Initial testing demonstrates that the seal is successfully established within seconds and mitigates blood loss at physiological levels over seven minutes, which could be the difference between life and death for a gunshot wound victim awaiting medical care.

Valera IUD

Hilme Athar, Darren Dong, Elisa Fang, Alex Kim, Lillian Wang

Advisors: Prof. Nandan Nerurkar & Prof. Kristin Myers

The intrauterine device (IUD) is the leading form of reversible contraception, with over 99% effectiveness and 168 million users worldwide. However, current IUD options have a one-size-fits-all shape and size that results in IUD expulsion from the uterus in up to 10% of users. IUD expulsion often goes unnoticed, leading to ineffective contraception and high risk of unplanned pregnancy. IUD users need a novel IUD design that remains in the uterus regardless of intrauterine forces and variations in uterine size and shape. Our solution, Valera IUD, solves the problem of IUD expulsion. Valera IUD is a blossom-shaped IUD which conforms to the uterus upon deployment and can decrease expulsion rates through a more adaptable fit. Initial prototype testing shows that our design is able to take on a wider range of conformations than current market IUDs and withstands uterine forces at levels comparable to existing IUDs, making the Valera IUD a promising approach to mitigate IUD expulsion.

Circuvent

*Abhishek Chakraborty, Chandana Golla, Audrey Lee, Qiyue Peng, Mojde Yadollahikhales
Faculty Advisors: Prof. Katie Reuther*

The recommended treatment for a subset of mechanically ventilated COVID-19 patients is to place them on their belly. This practice is called prone positioning therapy; however, the manipulation of the endotracheal tubing (ETT) during repositioning presents the clinical challenges of (1) being dangerously kinked or dislodged, (2) being difficult to work with during emergency situations, and (3) increasing potential exposure of health workers to aerosolized infectious agents. Our solution can be directly connected to the mechanical ventilator and consists of a loop with ports throughout its circumference to facilitate connections to the ETT in a variety of patient positions. When a patient must be rapidly flipped, the patient remains intubated while the ventilator and vacuum hoses can be quickly re-positioned, and the patient rotated without requiring complete reconstruction of the entire apparatus. Our solution effectively protects patients and health care workers from dislodgement of the ETT and enables rapid medical intervention, while minimizing the risk of exposure to healthcare providers.

NeuroTrak

*Brandon Cuevas, Abhinav Kurada, Panagiotis Oikonomou, Juan Rodriguez
Advisor: Prof. Katie Reuther*

Epilepsy is a neurological disorder that affects over 65 million patients worldwide. Currently, the cycle of care for epilepsy is hamstrung by physician's over-reliance on inaccurate self-reported seizure data for monitoring patients outside-the-clinic. Over 85% of seizures go undetected in patient self-reporting. As a result, physicians often do not have sufficient data to confirm whether the medication they prescribed is effective in reducing seizures, leading to millions of patients experiencing a multi-year lag between initial diagnosis and optimal treatment.

NeuroTrak aims to address this need by designing an outpatient solution to detect and differentiate focal onset with impaired awareness seizures (FIAs), the most common seizure subtype. Our wireless EEG system continuously gathers patient data, streams this biosignal to the patient's phone, and classifies this EEG data in real-time. Through our Residual Neural Network technology, Neurotrak will quantitatively inform clinical decisions through its 77% FIA detection and 85% seizure differentiation accuracy.

ViveSense

*Benji Greenfield, Dvora Leibowiz, Rosy Li, Peyton Peng, Jeremy Perna
Advisor: Prof. Qi Wang*

A growing fraction of the global population faces infertility issues. Nearly half the cases of infertility are attributable to the male's reproductive system; treatments are often delayed due to the flawed assumption that the female partner is the infertile. Many men, including those who are recommended by physicians, do not seek reproductive healthcare because tests are costly, inaccessible, and socially awkward. Current at-home test kits are not accurate or readily interpretable by users. ViveSense presents a comprehensive, digital, at-home solution for aspiring fathers. A user collects a semen sample that he inserts into a cell-phone add-on optical system that captures video of the sample. Our image processing algorithms analyze the video and calculate key sperm health metrics. A cell-phone application outputs the results to the user and monitors health over time, providing an accurate, easily interpreted assessment of sperm health.

Solair

*Lynn Bi, Bunmi Fariyike, Asad Saleem, Chris Shen, Karina Yeh
Advisor: Prof. Kristin Myers*

According to the World Health Organization, lower respiratory infections are the leading cause of death in low-income countries. Moreover, the co-morbidity of these diseases with the novel coronavirus has and will continue to devastate countries in all developmental phases. Studies estimate that 55% of these deaths could be prevented by providing consistent access to oxygen with breathing assist devices. However, current oxygen delivery methods are insufficient, requiring either cumbersome oxygen cylinders or expensive, high-maintenance, and electricity-dependent oxygen concentrators. Solair aims to provide a low-cost oxygen source with off-grid functionality and the necessary robustness for low-resource and/or emergency settings. We accomplish this by modifying the design of current concentrators to include pneumatic instead of electric valving components and by adding a solar-powered charging module. Computational simulations and in silico calculations demonstrate that Solair's novel pneumatic valve system and partially solar-powered paradigm show promise for generating oxygen of comparable quantity and purity to that of standard concentrators.

ABW

*Michelle Borovskoy, Sam Jennings, Carlos Perez, Milcy Perez, Kylee Sullivan
Advisor: Prof. Christoph Juchem*

IV infiltration and extravasation are complications that occur when fluid from a peripheral IV is not delivered into a blood vessel but instead leaks into the surrounding tissue. If undetected, severe tissue damage may occur. It is estimated that there are about 47.8 million cases in the U.S. each year.

Diagnosis of such events is reliant on medical staff observation of the area surrounding the IV injection site. The lack of standardized, quantitative, continuous monitoring contributes to the diagnostic deficit, leaving IV patients susceptible to inadequate therapy or injury.

Our proposed solution enhances medical staff's observational capability by detecting swelling, temperature, and discoloration at the IV site that are indicative of infiltration or extravasation. Our initial testing shows that our sensors have sufficient sensitivity for early detection of an event.

Get Pumped

*Michael Anne Bolene, David Carratu, Maria Geraghty, Hunter Hasley, Sarah-Jane Lynn,
Kelsey Troth*

Advisor: Prof. Gerard Ateshian

Every day, up to 49% of women in America make a conscious decision to slip on a pair of painful high heels, which disrupt the natural mechanics of the body leading to long-term effects such as toe abnormalities, bunions, nerve damage, and arthritis. Although 71% of women report pain from their heels, they continue to wear these uncomfortable but fashionable accessories. Current solutions such as insoles, moleskin, or detachable heels only provide temporary relief from the inherent design flaws at the root of the problem. Get Pumped offers a revolutionary high heel carefully attuned to biomechanical stresses on the body, designed and tested with the goal of improving gait patterns and reducing damage through the use of mechanical dampeners in the heels, non-Newtonian soles, and a continuous linear incline build. We offer a biomechanically-sound alternative for health-conscious people without sacrificing the aesthetic appeal of high heel shoes.

You-V Safe

*Nitya Hinduja, Jordynn Lurie, Mariel Ogurek, Lola Omokanwaye, William West
Advisor: Prof. Barclay Morrison*

The current COVID-19 outbreak has mandated extended use of N95 masks. Medical personnel may touch their mask more than 25 times during extended use, introducing the possibility for contact transmission of pathogens between patients or during doffing of their masks. Current mask decontamination methods take too long and require healthcare workers to remove their mask. We present a decontamination hood for healthcare facilities that will allow for safe extended mask use by decontaminating N95 masks throughout the course of a day, reducing the risk of spreading pathogens and reducing mask degradation. The resultant design superposes 222 nm UVC sources, allowing uniform spectral irradiance within a 10 cm region of interest for 30 second exposure periods. This wavelength and dosage have been proven to effectively decontaminate N95 masks and retain mask integrity while being safe for prolonged human exposure. Healthcare workers can clean their masks without removing them and with minimal disruption to their daily routine.

Clear Vision

*Steven Bessler, Jonathan Kapilian, Michael Kirschner, Moshe Willner, Lekha Yesantharao
Advisors: Prof. Nandan Nerurkar*

During laparoscopic surgery, the laparoscope's lens can be obstructed by debris, blood, interstitial fluid, or condensation. The surgeon must remove the scope from the body and clean the lens approximately twelve times per hour of surgery. This prolongs procedure time and costs the health-care system approximately \$255.3M annually. Many solutions fail to clear obstructions, or have limitations such as manual intervention, reduced dexterity, increased bulkiness, or sutured components. Therefore, there is a need for a way to maintain a clear visual field during laparoscopic surgery with minimal disturbance to the surgeon's concentration. Clear Vision is a novel solution to this problem. The small cap rests on the lens of the laparoscope and detects obstructions using an infrared sensor. This initiates bursts of pressurized saline and CO₂ to clear the obstruction. Initial prototyping and testing demonstrated effective detection and efficient cleaning without interruption to the surgery's progress.

Mask On

Grace Kim, Yujin Kim, Christina Li, Helen Xu, Hangwei Zhuang

Advisor: Prof. Clark Hung

N95 respirators are crucial in protecting health care workers (HCWs) from potential COVID-19 transmission. The personal protective equipment shortage has forced HCWs to decontaminate and reuse respirators. However, mask fit degrades quickly with 20% failing fit tests after five decontamination cycles, exposing HCWs to 30% more ambient aerosols than properly fitted masks.

Infected HCWs put themselves, colleagues, and patients at risk. Currently, no solutions improve respirator fit to extend its use. Therefore, a solution adaptable in-hospital that prevents air leakage when HCWs wear respirators is needed. We propose an elastic harness that fits over and around a respirator, with straps holding the mask flush against the face. An air-filled flap folds under the nose bridge for improved seal and comfort. A fluorescent tracer test will quantify our solution's impact and the total inward leakage (TIL) of the modified mask will be quantified using an OSHA-approved aerosol test.

CIVIL ENGINEERING AND ENGINEERING MECHANICS

Re-imagining Green Spaces

https://www.youtube.com/watch?v=xpv_UMtAKwM

Jackson Burdett
Sarah Kane
Ollie Schuster
Emily Su
Alexandra Wagner

Re-imagining N.Y. Stewart International Airport

<https://www.youtube.com/watch?v=05xDo9sJrXw>

Daniel Barberena
Christopher Kumaradjaja
Erik Melicio
Anthony Nie
Isabel Weil

Long Island Community Center

https://www.youtube.com/watch?v=QHOz9G6Pz_8&t=20s

Simon Chamorro
Roberto Interiano Jr.
Anshuman Kowtha
Jhon-Carlo Marroquin

Hudson River Pedestrian Bridge

<https://www.youtube.com/watch?v=6tjW7mYWPQ&feature=youtu.be>

Alejandro Samper
Jaime Danies
Matias Molina
Alejandro Quintana

Duffield House

**A Living Learning Community and Student Accommodation
NYU Tandon School of Engineering, Brooklyn, NY**

<https://www.youtube.com/watch?v=Z7iJ3IAmvSk&t=>

Kara Fragola
Ally Israel
Nimat Maloney
Abigail Roberts
Clare Chan

Under One Roof – McCarren Park Stadium Design

<https://www.youtube.com/watch?v=v5ahaoM3B4w&feature=youtu.be>

Monte Cardenas-Metal
Xinyi Hu
Ravi Jalan
Mackinley Wang-Xu

CHEMICAL ENGINEERING

**ChemE Five Guys Co.
Methanol Unit Design Presentation**



Tucker Burg
Andrew Palacios
Matthew Gonsalves
Max Miloslavsky
Chang M Yun

ELECTRICAL ENGINEERING

Columbia University Formula Racing EV21 Design

Bernard Steyaert, Myles Barrow, Youssef Fahmy

Matthias Preindl - Electrical Engineering

The goal of this project is to design the electrical systems of the Columbia University Formula Racing (CUFR) 2021 electric vehicle (EV). This project implemented several improvements over the 2020 EV including a modular battery management system (BMS), a redesigned high voltage (HV) system featuring a new accumulator and electronics, and an optimised low voltage harness with modularized microcontrollers.

The modularized BMS was a custom design created to track the voltage and temperature of each of the 72 Energus Li2x8pVTC5AT battery cells, as well as communicate with other systems of the vehicle such as the shutdown circuit and the charger. This was achieved using a combination of PCBs and microcontrollers. Six PCB monitoring boards and a centralized master board were designed. Each board features a microcontroller, the monitoring boards use Arduino Micros and the master board uses a Texas Instrument C2000 Delfino, which were programmed for the aforementioned functions. Other new features over the previous design include control of the Accumulator Isolation Relays (AIRs) and the cooling system. Having a custom-made design allowed the 2021 BMS to be a more robust and easily integratable system.

The HV system improvements over the previous year's design include a new inverter, battery enclosure, and better-suited components. The Cascadia PM100DX inverter was selected for its reliability. The HV enclosure was expanded from a simple

accumulator, housing the batteries and some electronics in the 2020 design, to now include the entire HV system. This includes the inverter and all of the HV components, from disconnects to safety circuitry, except for the Emrax 208 medium-voltage motor and its three-phase AC cables. The batteries are configured into six segments of 12 batteries each, and are easily removable and serviceable. Other new components that were designed and selected include the HV fuse, indicator lights, energy meter, and safety circuitry. Calculations were also performed to validate the motor performance and gear ratio between the motor and differential. The basis for an open-loop traction control algorithm was implemented as well.

The low voltage systems of the vehicle revolve around four enclosures, each with its own PCB and direct wire-to-board connectors. Fusing is decentralized, with each enclosure containing its own fuse box to power its internal components and peripherals. All signals that are allowed by the rules to be on the single digital bus are, minimizing wiring.

A 300W liquid and air cooling system is powered by a DCDC converter, drawing power from the HV battery pack, keeping the inverter, motor, and batteries well below the required 60C.

The shutdown circuit (SDC) and brake system plausibility device (BSPD) PCBs, which shield-mount directly into the enclosure PCBs, include only the bare essential SMD components, reducing their size.

References

[-https://www.fsaonline.com/cdsweb/gen/DocumentResources.aspx](https://www.fsaonline.com/cdsweb/gen/DocumentResources.aspx)
[-http://formula-hybrid.org/wp-content/uploads/2020-Formula-Hybrid-Rules-Rev-1-1.pdf](http://formula-hybrid.org/wp-content/uploads/2020-Formula-Hybrid-Rules-Rev-1-1.pdf)
[-https://wisconsinracing.org/s/WR-217e-Architecture-Design.pdf](https://wisconsinracing.org/s/WR-217e-Architecture-Design.pdf)

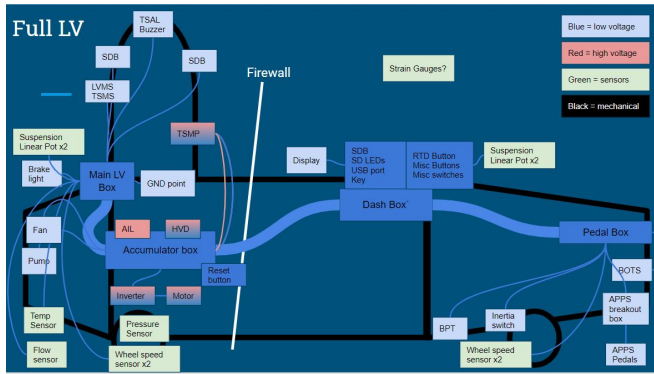


Figure 1: Block diagram showing component placement

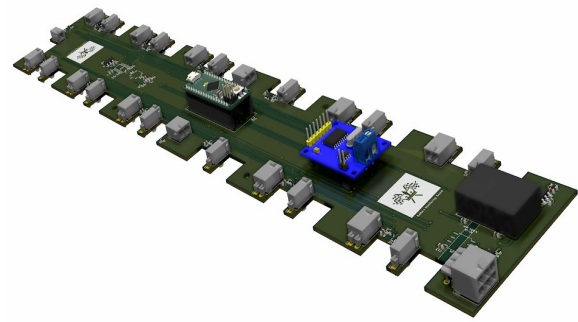


Figure 2: BMS monitoring board, Sabin Zarrandikoetxea

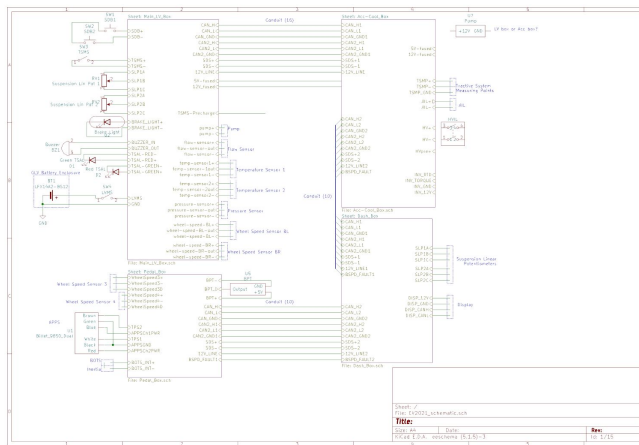


Figure 3: Electrical schematic of vehicle

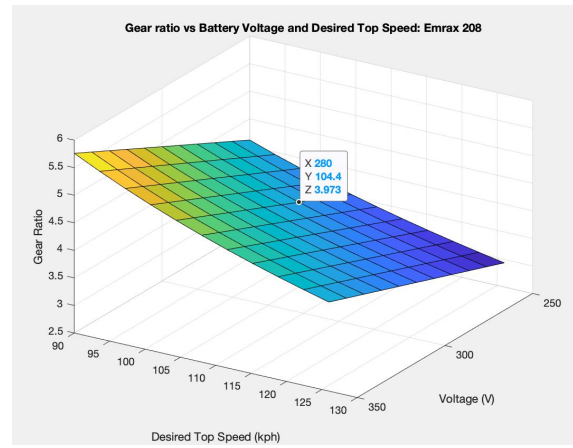


Figure 4: Gear Ratio vs Battery voltage and Desired Top speed for Emrax 208

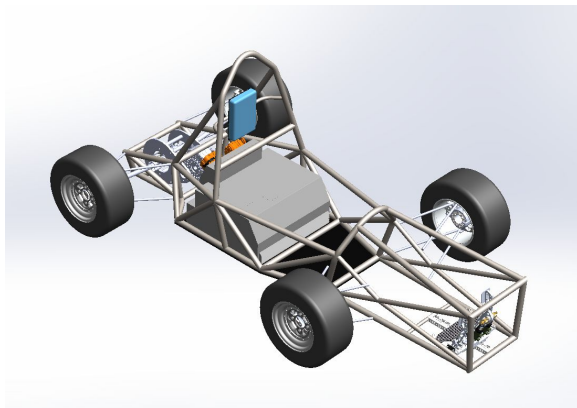


Figure 5: Figure: Protope CAD model of vehicle, Mikhail Sigalov, Andrew Chuka, Alfonso Ussia

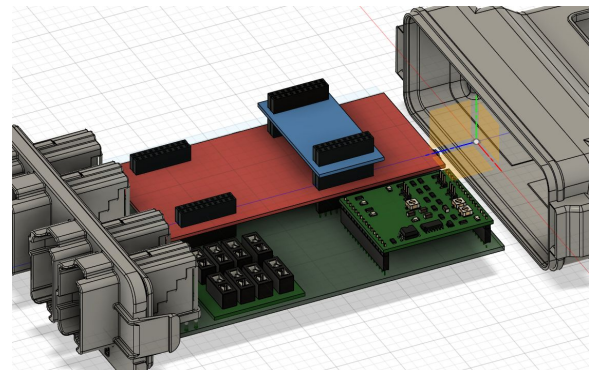


Figure 6: Low voltage enclosure with TI C200, fuses, and shutdown circuit. Tyler Riddle.

Brain Maze: 2-D Virtual and Physical Vehicle Navigation using Thoughts and Words

**Cory Langrey, Kaylo Littlejohn,
Peter Mansour, Jiaang Yao**

Advisors: Vinay Raghavan, Prof. David Vallancourt and Prof. Nima Mesgarani,
Department of Electrical Engineering

With rapid developments in the nascent field known as brain computer interface (BCI), “from thought to action” is no longer a wild dream for humans. BCI allows us to decode the thoughts and intentions of people via recording brain signals and analyzing them in real-time. In the meantime, speech processing has become more commonplace within our lives, enabled by the recent boom in deep learning. In this project, we used the BCI paradigm known as P300 speller and speech recognition using neural networks to allow multimodal control of robotic vehicles within either a physical maze or a 3-D virtual maze in Unity [1, 2]. User inputs from the two control modes, which form the input module of the project, were sent to a central module that handles the game logic and sets up TCP servers to allow simultaneous control of multiple users. The central module then communicates with the maze module, and the intended commands are executed by vehicles in either a virtual maze or a physical honeycomb-shaped maze.

The input module can either run the P300 speller paradigm using the BCI2000 program or the speech recognition module to predict the intended Left/Right movements for the vehicle based on the user’s thoughts or speech. The P300 speller paradigm deduces intended thoughts via the neurological phenomenon that humans will produce different brain signals when they see infrequent target stimuli interspersed within a series of more frequent irrelevant stimuli. In our project, the P300 paradigm was modified such that players can control the movement by silently counting the

number of flashes of L/R letters they see on the screen. The speech recognition module uses neural networks to analyze and classify speech input of the user robustly in real time [3].

The central module consists of scripts that extract the maze outline from images, load the maze game, track players’ positions, detect collisions, and update the user interface. It employs a TCP network, which allows for sending and receiving of serialized objects holding base64-encoded images, gameplay, and commands, to manage the communication between players, clients outside the game network, and the server. The central module also supports communication over RFCOMM bluetooth for exchanging messages with the bluetooth-controlled vehicles.

The final maze module consists of the Unity3D environment and the physical setup, which operate in parallel to each other but in series with the overall system. Both take commands from the central layer, but the Unity3D environment uses AI to control virtual vehicles through a series of waypoints and the physical robot traverses a real map using line following.

Due to restricted access to lab equipment given the ongoing pandemic, we demonstrated our project using simulated brain signals and actual speech input. Ultimately, the physical robot showed the desired results and was able to follow and turn according to the desired commands. The Unity3D paradigm, although working correctly with a set of test inputs, had trouble connecting with the middle layer and ultimately the two modules could not connect and communicate properly.

References:

- [1] Rezeika, Aya, et al. "Brain-computer interface spellers: A review." *Brain sciences* 8.4 (2018): 57.
- [2] Reddy, D. Raj. "Speech recognition by machine: A review." *Proceedings of the IEEE* 64.4 (1976): 501-531.
- [3] de Andrade, Douglas Coimbra, et al. "A neural attention model for speech command recognition." *arXiv preprint arXiv:1808.08929* (2018).

Device for Early Detection of Bedsores

Adina Becchofer, Megan Noga

Advised by Prof. Kymissis, *Department of Electrical Engineering*, Columbia University.

Bedsores are a type of pressure injury prevalent in bed-bound hospital patients and individuals in wheelchairs. They develop as a result of consistent pressure applied to the blood vessels in the dermal tissue, usually by bone mass. The pressure prevents normal blood perfusion in the skin layers, which causes the oxygen deprived cells to die off. Visible symptoms include red irritated skin in mild cases and dark blue or black painful spots in more severe cases. The severity of the injury can range from causing extreme discomfort to being life threatening, depending on the progression of the tissue necrosis. Because symptoms are most prominent after tissue damage has already occurred, early intervention is not always possible, and treatment is less effective and more expensive for advanced-stage bedsores.

Here, we present a design for a device that aids in the prediction and early detection of bedsores. In the medical use case, the device includes an array of sensors measuring capacitance, heart-rate, and blood-oximetry levels that are mounted to a flexible circuit board. The circuit boards are in turn embedded in a mattress cover that a patient lies on while the device tracks changes in blood flow throughout the body. To reduce the cost of production, the sensors will be located in areas where bedsores are likely to occur in supine patients, including the hip region, scapulae, and heels. We have created a scaled-down version of the aforementioned device as a proof of concept (**Figure 1**).

Hardware description: This design consists of 12 Maxim Integrated MAXREFDES117# boards that are arranged to be in contact with high-pressure regions of the subject's fingertips and palm (**Figure 2**). The chips on these boards

calculate heart-rate and pulse-oximetry by shining an LED into the skin and measuring the intensity of light reflected back into a photodetector. To reduce power consumption and proximal interference, time division multiplexing via decoders allows only 3 sensors to receive power at a time. Communication with the sensors is established through an I²C bus controlled by a microcontroller, and analog multiplexers allow the microcontroller to read data from only the boards that are currently powered (**Figure 3**).

Software description: The

MAXREFDES1173's developers, Maxim Integrated, supply Arduino-compatible starter code that samples the photodetector output at a rate of 25 Hz and calculates heart-rate and blood SO₂ saturation levels. This code's sampling parameters and calculations are modified to yield more precise and informative data and to account for the multiplexed sensors. Computed heart-rate, SPO₂, and tissue perfusion levels are displayed on a color-scaled visual interface (**Figure 4**). Such a data map for the full-sized device would assist healthcare providers in efficiently and proactively evaluating a bed-bound patient's risk for bedsores.

References:

- [1] S. Bhattacharya, "Pressure ulcers: Current understanding and newer modalities of treatment," *Indian J Plast Surg*, vol. 48(1), pp. 4–16, Jan-Apr. 2015.
- [2] T. E. Kurt, "SoftI2CMaster", 2010- 2012, hosted on Github, <https://github.com/todbot/SoftI2CMaster>.
- [3] H. Yamazaki, J Nishiyama, T Suzuki." Use of perfusion index from pulse oximetry to determine efficacy of stellate ganglion block," *Local Reg Anesth*. Vol. 5, pp. 9-14, Mar 2012.
- [4] "MAXREFDES117#: Heart-Rate and Pulse-Oximetry Monitor," hosted on Maxim Integrated, <https://www.maximintegrated.com/en/design/reference-design-center/system-board/6300.html>.
- [5] J. Valdez and J. Becker, "Understanding the I²C Bus," hosted on Texas Instruments, Jun. 2015, <http://www.ti.com/lit/an/slva704/slva704.pdf?ts=1589521293457>.

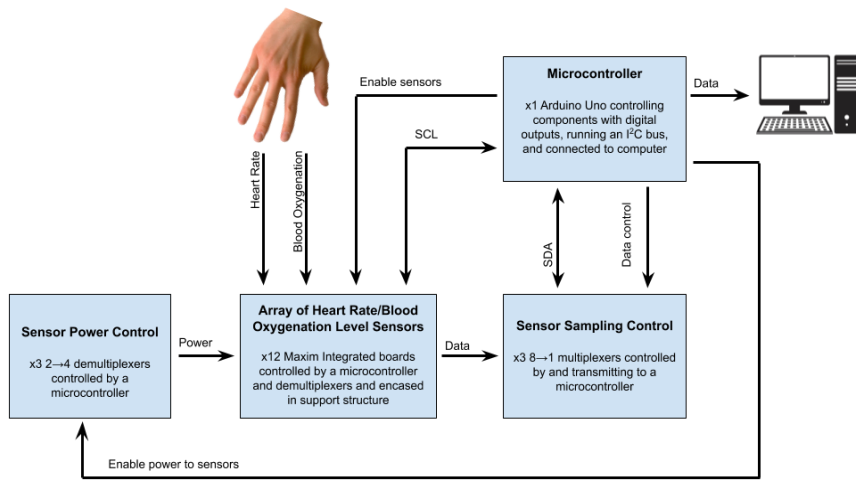


Figure 1: System block diagram showing the data's progression from hand to computer.



Figure 2: Red x's represent the sensor locations. Sensors are located in the pressure points of the fingertips and palm.

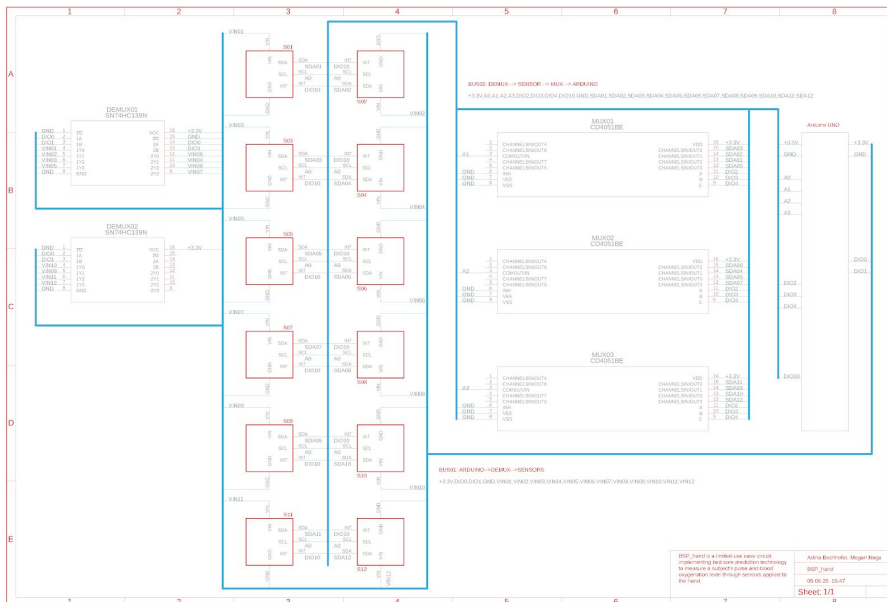


Figure 3: Circuit schematic for hand-sized detection device. Design blocks (left to right): demultiplexers, sensors, multiplexers, microcontroller. Zoom to view individual connections.

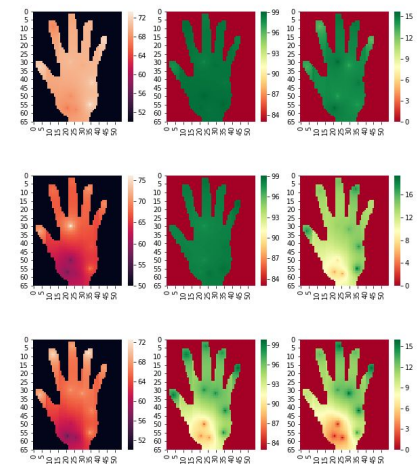


Figure 4: Screen captures of visual interface showing simulated heart rate (left), SPO_2 saturation (middle), and perfusion index readings over time when consistent pressure is applied to the right lower palm.

Digital Food - Laser Cooking

Gabriel Seymour

Dr. David Vallancourt, Electrical Engineering Department

Cooking has been an analog process since its discovery nearly 1.9 million years ago. At its first inception, cooking was a breakthrough technology that allowed people to spend less time eating and more time doing other things [1]. The Digital Food project of the Creative Machines Lab at Columbia University aims to make cooking even less of a hassle by minimizing user interaction with the food before it is ready to eat. One way in which we are taking the user out of the cooking process is by cooking with lasers.

Typical cooking processes have low-resolution spatial and temporal control; energy is provided by the heating of entire cooking chambers or cooking platforms and real-time feedback is hard to receive due to the high temperatures of either type of cooking apparatus. Lasers provide high-resolution axial control by providing energy only in extremely localized areas where the laser is incident on the material. High-resolution lateral control is provided by choosing a laser wavelength with a specific absorption in water; wavelengths with higher absorption in water are better suited to cook the surface of food whereas wavelengths with lower absorption in water are better suited for penetrative cooking. For example, a carbon dioxide (CO₂) laser with a wavelength of 10.6 μm has a significantly higher absorbance than a gallium nitride (GaN) laser diode with a wavelength of 445 nm, thus making the CO₂ laser better suited for surface cooking [2] and the GaN laser better suited for penetrative cooking. Using a Raspberry Pi 3 Model B (Raspberry Pi, Cambridge, England), two digital-to-

analog converters (Adafruit, New York, United States), and dual-axis mirror galvanometers (Seed, Shenzhen, China), we are able to selectively laser cook food [3]. Furthermore, by using a thermal camera (FLIR, Oregon, United States), we are able to receive real-time measurements of the average temperature of the food as well as point-by-point temperature measurements of the food surface. By periodically taking images of the surface of the food, we are able to find the minimum temperature spot of the food and use a greedy algorithm to cook that spot. This process is repeated until the desired temperature of the food is reached, thus achieving autonomous laser cooking and taking out the user from the cooking process.

Acknowledgements:

Thank you to Ph.D. candidate Jonathan Blutinger and Professor Hod Lipson for their continuous support over the last two years.

References:

- [1] C. Organ, C. L. Nunn, Z. Machanda, and R. W. Wrangham, "Phylogenetic rate shifts in feeding time during the evolution of homo," *Proceedings of the National Academy of Sciences*, vol. 108, no. 35, p. 14555–14559, 2011.
- [2] J. D. Blutinger, Y. Meijers, P. Y. Chen, C. Zheng, E. Grinspun, and H. Lipson, "Characterization of co2 laser browning of dough," *Innovative Food Science Emerging Technologies*, vol. 52, p. 145–157, 2019.
- [3] J. D. Blutinger, Y. Meijers, and H. Lipson, "Tandem laser system for highly tunable cooking and browning of food," Oct. 18 2017. United States provisional patent pending under application #62/573,765.

Filter Design using Genetic Algorithms

Jarrett Ross, Graham Stubbs

Prof. David Vallancourt, Electrical Engineering

Analog filter design is a well-known problem in the field of electronic circuit design. Genetic algorithms, a class of optimization algorithms based on biological processes, can be used to design analog filters that meet appropriate benchmarks.

In this paper, we describe a genetic algorithm that was used to design passive analog filters meeting a variable set of specifications including filter order, component types, passband and stopband frequencies. Additionally, the algorithm can be used to design a circuit to mirror a given frequency response from an existing filter.

Circuits were constructed in pre-designed “embryos” [1] made of a voltage source and load resistor (Fig. 1). The genetic algorithm circuit is constructed in between the input and output nodes marked in Fig. 1. These components are considered unmodifiable by the algorithm.

Circuits in the algorithm are represented as binary trees [2] (Fig. 2). In these trees, leaf nodes represent a specific passive component and inner nodes represent the configuration between its two child nodes. Resistors, capacitors and inductors were used as the components. The configurations used were series, parallel, series with ground and parallel with ground. The series configuration represents a construction of its two child components (or subtree of components) in series while ground series represents a construction of its two child components in series with ground (Fig. 3). The parallel and ground parallel configurations are analogous.

The genetic algorithm uses crossover, mutation and selection as its main functions for driving evolution. Initially, a population of N individuals is created, each representing a specific circuit. Note that since these circuits are randomly generated, most of the circuits in the initial population are invalid circuits and not able to be simulated. However, even if a circuit is not able to be simulated, it still might contain subcircuits that could potentially contribute to a valid circuit. The initial population is then

copied into a child population. Crossover, mutation, fitness calculation and selection are then performed, in order. After selection, the chosen individuals form a new generation and undergo the same procedures as the parent generation. This loop continues until a satisfactory number of generations have been evolved or fitness criteria achieved.

Single point crossover was used as the crossover method. A single node was chosen in the circuit tree of an individual and its subtree was swapped with the same subtree in another individual.

A mutation involved a node in the circuit tree of an individual changing its type (e.g. from series to parallel or resistor to inductor) or its value (e.g. from $10K\Omega$ to $1K\Omega$). A node could also be added or removed.

Ngspice was used to calculate the frequency response of each individual. The Ngspice response was compared with the ideal filter frequency response using root mean square error and assigned this value as its fitness.

Tournament selection with one elite child was used for the selection process.

Our algorithm was able to evolve up to 4th order lowpass, highpass and bandpass filters. An example of a simple 1st order bandpass filter is shown in figures 4 and 5. A 4th order lowpass filter is shown in figures 6 and 7. The best circuit evolved in generation 18 of the same trial as the 4th order lowpass is shown in figures 8 and 9 to show the evolution between an intermediate circuit and the final circuit.

References

[1] Koza, John R., et al., “Genetic Programming III” p. 392-502, Morgan Kaufmann, San Francisco, 1990.

[2] Lipson, Hod. “Genetic Programming”. Evolutionary Computation & Design Automation. Columbia University. 2019. Lecture.

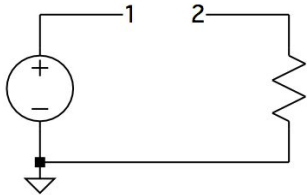


Figure 1. Embryo circuit. Not shown are potential evolvable connections to ground.

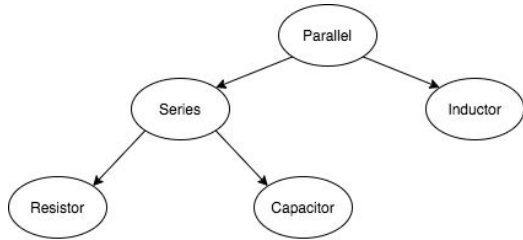


Figure 2. Example of circuit tree representation.

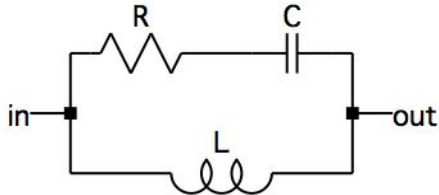


Figure 3. Circuit formed from circuit tree in figure 2.

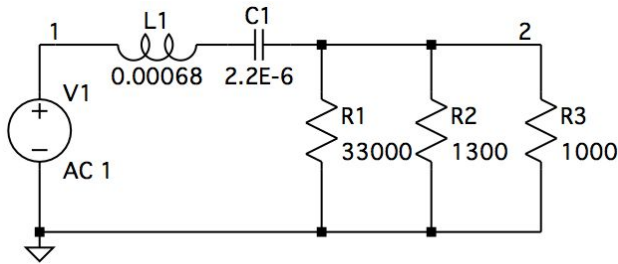


Figure 4. 1st order bandpass filter, evolved in generation 284 of a trial with a population size of 300. Note that similar components in series and parallel have not been simplified to emphasize the structure of the genetic algorithm circuit tree.

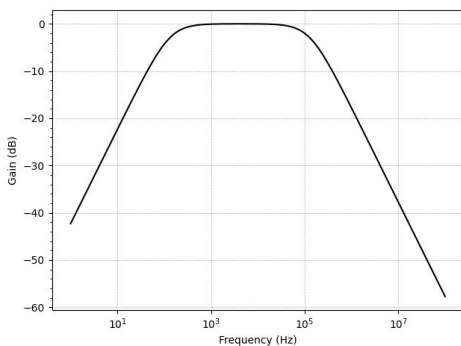


Figure 5. Frequency response of the 1st order bandpass filter depicted in figure 4. The filter was evolved to have corners at 100Hz and 100KHz.

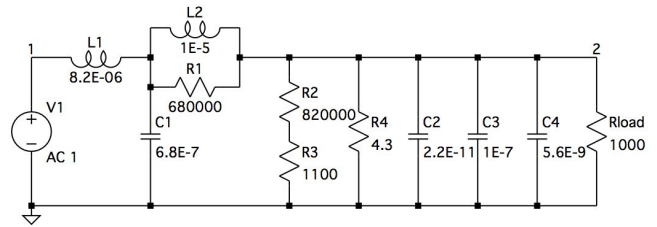


Figure 6. 4th order lowpass filter with corner at 100KHz. Evolved in generation 321 of a trial with a population size of 300.

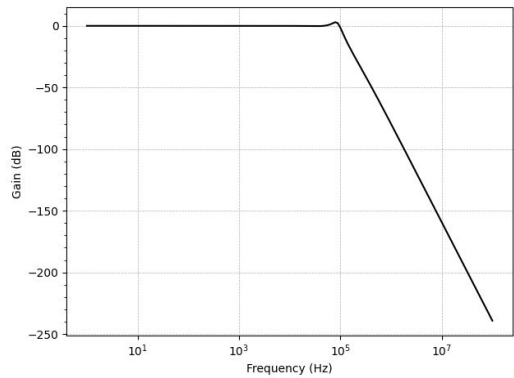


Figure 7. Frequency response for the 4th order lowpass filter depicted in figure 6.

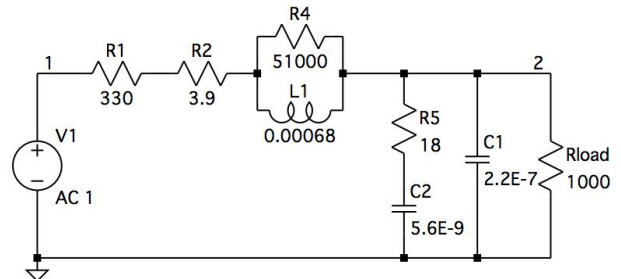


Figure 8. Best of generation schematic for a 4th order lowpass filter evolved in generation 18 of the same trial as the filter in figures 6 and 7.

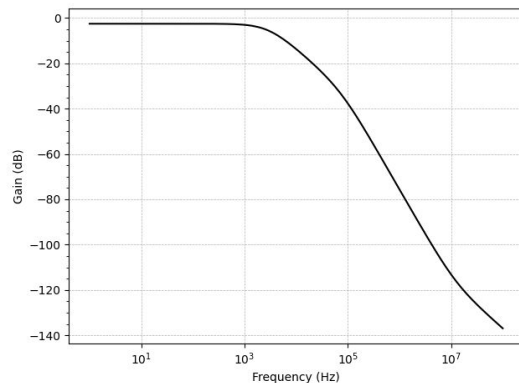


Figure 9. Frequency response for the filter depicted in figure 8. Note the general shape of the response is correct but the corner and roll off are not at acceptable levels yet.

Fourier the Artist

Jamie Mullins, Haley So

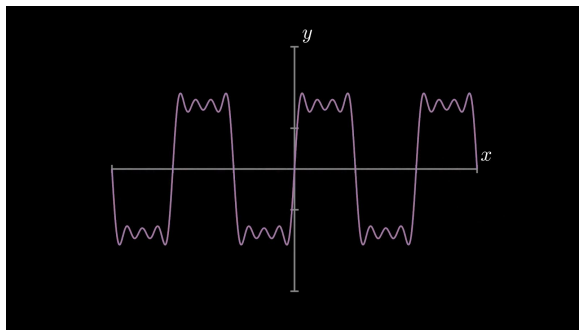
[Quip doc](#)

Let's say I give you a slice of cake I baked. I know the recipe, but you do not. But what if I asked you to figure out what ingredients and exactly how much of each ingredient was used to create the cake? That seems like a pretty difficult task.

That's essentially what the Fourier transform allows us to do with seemingly complicated signals. All signals can be decomposed into sine waves of different characteristics: amplitudes, frequencies, offset etc. The Fourier transform allows us to represent a waveform in not only the time domain, but now also the frequency domain.

Take a look at a waveform electrical engineers know well, the square wave. In the animation, we just show up to the 4th order sine wave. If we add more orders, it will become a much cleaner square wave.

$$sq(t) = \frac{4}{\pi} \sum_{n=1,3,5\dots}^{\infty} \frac{1}{n} \left(\sin\left(\frac{n\pi x}{L}\right) \right)$$



The Math

Any periodic signal can be created with just sine waves.

$$X_k = \sum_{n=0}^{N-1} x_n e^{-i2\pi k \frac{n}{N}}$$

$$X_k = \frac{1}{N} \sum_{n=0}^{N-1} x_n e^{i2\pi k \frac{n}{N}}$$

This is the equation for the discrete Fourier transform and the inverse Fourier transform. When the former is applied to a wave in the time domain, it outputs the strengths of its frequency components in the frequency domain. The Fourier transform works on periodic signals (and if they're not, in practice, we just loop it to make it periodic). One way to think about what the Fourier transform as described by 3Blue1Brown is by wrapping your periodic function around the origin. The center of mass will stay roughly around the origin, that is until we spin at a frequency that lines up with one of our components. So for example, if we have some amount of a 5Hz sine wave and we spin the graph around the origin at 5 revolutions per second, all the points in the 5Hz sine wave will line up, pulling the center of mass out from the origin on to a number on the positive x-axis, which corresponds to the amount of the 5Hz that we have in the overall signal. Given frequencies, amplitudes, and phase, we can recover the original time domain signal with the inverse Fourier transform.

Using this idea, we can understand the equations above a bit more. We can extract the recipe by finding the amount of each frequency by spinning our signal around the origin at that particular frequency.

As electrical engineers, we use the Fourier transform for designing circuits, analyzing spectrosopes, any signal processing or work in communications, or imaging (to name a few), but Fourier transforms aren't just for the technically inclined. There are also some wonderful ways that Fourier transforms can be used in the visual and aural world. Inspired by 3Blue1Brown, we decided to bring out the beauty of this math, we worked to create drawings and art through the Fourier Transform while giving you more of an insight into Fourier.

Although our original senior design project was to showcase a few machines based on

Fourier to paint physical paintings and to create aural art for an art show, we are no longer able to do so due to COVID19. We will include sketches of our original plans, but please enjoy this digital art show.

Tools:

- Python
- Open source library manimlib

Using manim, we are able to create wonderfully smooth animations. In python, we take an image, convert it to svg so to extract a path, and from the path or rather this periodic signal wrapped around the origin, we can unwrap the signal, perform the Fourier transform to find the included frequencies, their amplitudes, and the phase. Taking these components, we rotate our circles of different radii at the given frequencies and phases to redraw the image. As you can see, as we increase the order, our image becomes closer and closer to the original. Alternatively, we can input a waveform and see the output, but in most cases, this just looks like a squiggle.

In playing around with representing the same shape at different orders of precision, we were exposed to some of the more subtle phenomena that characterize signal approximation not usually talked about in an introductory level signals class. For example, the prominence of the Gibbs phenomena was clearly seen in any image we attempted to recreate that included sharp edges or jumps. This phenomena, which explains the tendency or ringing about the edges of a square wave-like function to form high peaking “horns” even at high order approximation, can be seen clearly in the square wave example shown above. Related to this, we gained a more intuitive understanding of the tendency of Fourier coefficients to converge towards the actual much more quickly for smooth functions; this was contrary to our initial expectations in that we assumed that the most complex images, not those with the sharpest

edges, would be most difficult to represent in a fixed number of orders.

Hardware Plans:

By utilizing a set of functions derived from the manim library, we are able to obtain the set of frequency and vector length coefficients represented by k and x_n , respectively. These fixed values would then be translated to the physical machinery: the vector length would be manually adjusted by setting the appropriate length on the telescoping arm, and the frequency of rotation would be translated to the servo motor through the Adafruit Huzzah over WiFi.

We originally planned on configuring the Huzzah to execute Python code to compute the coefficients of the “arm” it was controlling locally, but quickly realized the microcontroller did not have the processing power to compute the mathematically intensive Fourier calculation code. Therefore, we developed a scheme for computing all terms on a central computer and using a basic web proxy to correlate the calculated rotational coefficients with the IP address of the associated controller to be sent over WiFi.

Art Show plans:

Our centerpiece was going to be this Fourier drawing machine giving a live demo as one showcase. We thought of a few variations, so our other pedestals would show the other mechanisms as well. We wanted to play with sound in the gallery and show how to morph sound with general signal processing to add to the art Fourier can create. All around the walls, we would have hung our artwork created by the machines.

Many analogies could be made between the mathematical properties of the transform and our artistic interpretation, such as line thickness corresponding to speed of rotation, color corresponding to order of the term, etc. to create a visually interesting representation.

Introducing Kükr: A New Platform for Video Recipe Creation and Sharing

Micah Roschelle¹, Noah Larky¹, Hana Mizuta², and Spencer Yen²

¹Department of Electrical Engineering, Columbia University

²Department of Computer Science, Columbia University

Email: mlr2194@columbia.edu, ndl2113@columbia.edu, hm2694@columbia.edu, ssy2121@columbia.edu

Abstract — In the wake of COVID-19, home-bound families have found emotional relief and social connection in cooking and sharing recipes. One popular form of recipe sharing has been through recipe videos. While a variety of existing platforms have been used to facilitate the creation and sharing of such recipes, no dedicated platform exists for these purposes. Here, we present Kükr, a dedicated and easy-to-use platform for video recipe creation and sharing. With Kükr, users can create Instagram-style recipe videos including necessary basic information, ingredients, and steps using an IOS-based phone application. These recipes can then be accessed by family and friends through a browser-based web application. This new modality for recipe sharing, we believe, is poised to propel the growing trend of collaborative cooking, and, thus, provide new avenues for social activity and creativity during this challenging time.

I. INTRODUCTION

The COVID-19 pandemic has forced millions in America and the world into social isolation, stirring up feelings of loneliness, fears of economic instability, and a public health catastrophe into an anxiety-infused concoction that some may call a recipe for disaster. In the face of these challenges, people around the world have taken to cooking and recipe sharing as a means for keeping their emotions to a simmer and fostering a dollop of social connection in these isolating times [1]. One popular medium for recipe sharing has been the video recipe. These recipes consist of short videos illustrating each cooking step and are often created and distributed on social media platforms such as Instagram or TicToc. These platforms, however, are designed for general video recording and do not have basic features that are necessary for creating or viewing a recipe, such as the ability to access an ingredient list and to review cooking steps or view them out of chronological order. Furthermore, they are only easily accessible by registered users, limiting accessibility.

To further facilitate the creation and exchange of video recipes we introduce Kükr, a dedicated recipe creation and sharing platform. With Kükr, users can create Instagram-style recipe videos including necessary basic information, ingredients, and steps using an IOS-based phone application. These recipes can then be accessed by family and friends through a browser-based web application that does not require any custom plugins or user registration. This new modality for recipe sharing, we believe, is poised to propel the growing trend of social cooking, and, thus, provide new

avenues for social activity and creativity during this challenging time.

II. IOS RECIPE CREATION APP

The recipe creation aspect of the Kükr platform is built into an IOS-based smart phone application. This application presents the user with an easy-to-use user interface for entering necessary recipe information and ingredients as well as filming video and writing text for individual recipe steps. The recipe creation page of the app is shown in fig 1.

The recipe creation process is segmented into three sections: overview, ingredients, and steps. In the overview section, the user enters basic information about the recipe such as cooking time, yield, and the recipe name. An ingredient list can be entered in the ingredients tab. And, finally, in the steps section, the user can enter text and record the associated videos for each step in their recipe.

For step creation, an intuitive carousel UI is implemented as seen in fig 1. Each step is represented as an element of the carousel, such that the user can easily move between successive steps and edit the steps in any order. To record a video, the user simply taps the carousel element and can choose to either upload an existing video from their camera



Fig. 1 Recipe creation page on Kükr IOS app.

roll or record a new video through the built in, IOS-like camera.

When the recipe creation process is complete, the user can return to the overview segment to upload their recipe to the Kloud. Upon uploading, the recipe is data is stored in a cloud-based database managed through Amazon Web Services. The user is provided with a unique URL link with which they can access and share their recipe using the browser-based recipe viewer.

III. BROWSER-BASED RECIPE VIEWING APPLICATION

Shared recipes can be viewed through Kükr’s browser-based recipe viewing application. This application allows the user to view the video recipe on the web through a custom user interface. An example recipe web-page is shown in fig 2.

On the recipe page, the basic recipe information and ingredients list are displayed in text. Each step is presented in a list of buttons. Whenever the user selects one of the step texts, the associated video plays to the right. In this way, users can easily re-watch recipe steps or look ahead to upcoming steps while following the recipe.

IV. CONCLUSION

Through its IOS-based recipe creation application and browser-based recipe viewing application, Kükr presents a new and intuitive means for users to easily create and share video recipes. We intend to launch Kükr on the app store soon after further user testing. Once launched, we hope Kükr will help facilitate social cooking for people of all ages and backgrounds as they learn to connect from a distance.

Banana Muffins

By Noah

Ingredients

3 Bananas
1/2 cup White sugar (scant)
2 Tbsp Butter, melted
1 Egg
1/3 cup Fat-free Greek yogurt
1 1/2 cup Unbleached flour
1 tsp Baking soda
1 tsp Baking powder
1/2 tsp Salt
optional Chocolate chips, to taste
2 Tbsp White sugar
3 Tbsp Packed light brown sugar

Steps

14: Scoop muffins
15: Combine white and brown sugars to make topping
16: Add topping and chocolate chips on top
17: Bake for 15 min then check every minute
18: Remove from oven and let cool (if you're patient enough)
19: Enjoy!!!!



Fig 2 Example of browser based recipe viewing application.

ACKNOWLEDGMENT

The Kükr team would like to thank Prof. David Vallancourt and the Columbia University Department of Electrical Engineering for supporting and guiding this project.

REFERENCES

- [1] N. Chittal, “Quarantine Cooking is about more than just feeding yourself,” *Vox*, March 27, 2020.

Phase Tracking Reference Signal Application in AWR VSS

Nicholas Kasseinov

Sponsored by AWR Corporation

Supervisor: Gent Paparisto

To increase protocol efficiency and to keep transmissions contained within a slot or beam without having to depend on other slots and beams, 5G NR (New Radio) introduces several new main reference signals. One of these reference signals is the Phase Tracking Reference Signal (PT-RS). Its main purpose is to track the phase of the local oscillators (LO) at both transmitters and receivers. By referring to the PT-RS, we are able to suppress phase noise and common phase error, which is especially prominent at higher mmwave frequencies.

The goal of this project was to identify the content of the PT-RS signal and understand how it could potentially be implemented into AWR Corp's Virtual System Simulator (VSS).

According to the 3rd Generation Partnership Project, the PT-RS symbols should be generated using a Gold Code [1]. Gold Code is a pseudo-random sequence of bits that is initialized according to some parameters specific to the context of the PT-RS' application, such as the slot number within a frame for a certain subcarrier spacing configuration or the given scrambling identity. To better understand the how the bits of the Gold Code are manipulated to give the PT-RS symbols, a MATLAB script was written. This script was then used as a reference to implement the PT-RS source into the VSS, as shown in Figure 1. This is, in essence, simply a physical manifestation of the MATLAB code. Other considerations, such as PT-RS time/frequency density, were implemented into the VSS by referring to information contained in "On the Phase Tracking Reference Signal (PT-RS) Design for 5G New Ratio (NR)." [2].

An example project was then built by Gent Paparisto with an OFDM modulator and demodulator and with the PT-RS placed in the proper locations. Phase noise was also inserted to distort the PT-RS symbols, which the demodulator used to produce an estimate of the transmitted PT-RS symbols. The demodulated data was used to estimate phase noise, which was applied to correct the remaining data.

Acknowledgments

I would sincerely like to thank AWR Corporation for their sponsorship on this project, especially Gent Paparisto.

References

- [1] 3GPP TS 38.211, "NR; Physical channels and modulation," 2018.
- [2] Qi, Yinan, et al. "On the Phase Tracking Reference Signal (PT-RS) Design for 5G New Ratio (NR)."

Pour-in, Pour-out Drink Chiller

Luis Collado, Mariana Fernandez,

Kyrelle Thomas

David Vallancourt, Electrical Engineering

I. Introduction

There are two common ways of making iced coffee: one can either chill hot coffee with ice or place it in a refrigerator. Each method requires a trade-off. Ice waters down coffee and refrigerating coffee takes time. We want to minimize that compromise.

II. Overview

The Pour In, Pour Out (PIPO) chiller has the capacity to cool down any hot beverage. To operate, a drink is poured into an aluminum tumbler that is then inserted into the chiller, where it will be surrounded by cooling plates. After selecting a desired temperature, the tumbler and the surrounding cooling assembly will be rotated until the beverage reaches the desired temperature. After two to three minutes, the user can remove the tumbler and pour out their chilled drink.

II. Components

The chilling system consists of three Peltier plates, semiconductor junctions that transfer heat when a voltage is applied. The thermoelectric cooling assemblies are arranged to transfer heat away from the aluminum tumbler, each via a heatsink and fan. To supply power to the plates while the container is in motion, a slip ring is used, with the rotating top being driven by a belt and a motor, and the static bottom connected to the power supply.

The device's rotational system relies on an aluminum tumbler that is shaped like a triangular prism. Flat walls maximize the surface contact between the tumbler and the cooling plates, and aluminum's high thermal conductivity promotes heat transfer.

Additionally, sharp corners in the tumbler wall create more turbulence in the liquid upon rotation, mixing the colder outer liquid with the warmer inner liquid more than with a circular tumbler. We opted for a removable tumbler over a fixed container after considering that cleaning after use becomes much easier with a single, removable, food-safe part.

Finally, the whole system is controlled by a Raspberry Pi 3 Model B. The Pi would have a program with a user-friendly GUI running on it that was written in Python. The program's inputs would be the user's desired cooling temperature, which the Pi gets from the touch screen, and the temperature of the chilling plates, which the Pi gets through temperature sensors. Based on the desired temperature and current temperature, the Pi will control the chiller's motor and the state of the chilling plates.

When voltage is first applied to the Peltier plates, they will begin to cool down. However, if they reach a temperature lower than 0 degrees, the system can be compromised. Thus, once the plates reach a temperature of about 3 degrees celsius, the Raspberry Pi will alternate between supplying and cutting off power to the plates to maintain them at that temperature. Once the plates reach equilibrium, the Pi will calculate the amount of time the system must run until the desired temperature is achieved, using a mix of experimental data and the initial temperature of the beverage. A solid state relay controls power to the cooling plates, ensuring a long product lifetime and noiseless operation during the cooling period.

References:

TEC Assembly: <https://www.adafruit.com/product/1335>

Retrobox

Jamison Bunge (jjb2230)
Allan Delarosa (ajd2215)
Jakub Ostrowski (jo2498)
Muhammad Aziz (maa2320)
David Vallancourt, Electrical Engineering

output from the microcontroller included a 3 channel equalizer. The circuit simulation also included the power amplifier that would have been used to power the speaker, providing a maximum of about +7dB in sound level.

Detailed Abstract

Retrobox is a privacy focused smart speaker. Devices like Amazon's Alexa give you the convenience of voice commands but with a steep trade off in privacy. Retrobox gives you the voice commands you'll actually use while cutting out the companies that want to collect your data. Since the device serves the purpose of a speaker without the privacy tradeoffs of modern day devices, we decided to model it after a boombox. This makes its functionality clear at a glance, and also gives it an "old school" feeling.

During the 2020 pandemic, building a physical device was no longer possible. Instead, we decided to simulate the experience of a boombox by building a virtual one on a web page. Some basic physical components, like the screen to display information and various buttons, could be implemented using software. Major hardware components could still be designed and then simulated using LTSpice. These SPICE simulations could then be used to process audio before being played on the web page and would allow for our project to still have some interaction between the software interface and the designed hardware components. A full breakdown of the software and hardware features we implemented can be found at <https://github.com/JamisonBunge/Retrobox>.

In order to give it the "old school" feel, the hardware responsible for processing the

Solar Microgrid Generator

William Meng, Alice Wu

David Vallancourt, Ioannis Kymissis,
Electrical Engineering

Perovskite Solar Cell Design

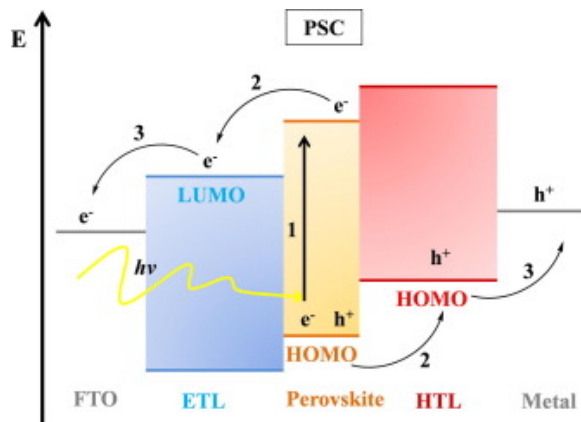


Figure 1. Energy diagram of perovskite solar cell layers [1].

Metal halide perovskites have demonstrated tremendous promise as a next-generation solar cell material due to its high defect-tolerance, long carrier lifetime, long carrier diffusion length, high absorption coefficient, and cheaper manufacturing process. The way perovskites solar cells work is similar to how any organic solar cell works. On the very top of the solar cell is a transparent conductive oxide coated glass, with the oxide serving as the top contact, while a metal, typically silver, on the bottom acts the back contact. Between these contacts lies an electron transport layer (ETL) and a hole transport layer (HTL) with the perovskite sandwiched in the very middle. The perovskite absorbs visible and ultraviolet light to generate electron-hole pairs. The ETL has a higher electron affinity and extracts electrons generated by the perovskite, while the HTL extracts the holes generated by the perovskite, thus splitting

the electron-hole pair and generating current, as shown in Figure 1.

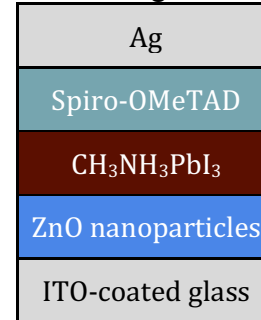


Figure 2. Solar cell device diagram. The solar cell would be fabricated in this orientation and then flipped with the glass side up when tested.

Our device materials and fabrication methods were based on literature and material availability within Prof. Kymissis' lab [2]. Though we were unable to fabricate the solar cells, the fabrication procedure would have been as follows. Beginning with an ITO-coated glass substrate, spin-coat a 6 mg/mL ZnO nanoparticle solution onto the substrate at 3000 rpm for 30s. Repeat three times to achieve a smooth film. A two step process will be used for the perovskite layer. First, spin coat a 460 mg/mL solution of PbI₂ in N,N-dimethylformamide on top of the ZnO at 3000 rpm for 15s. Once dried, immerse the substrate in a 10 mg/mL solution of CH₃NH₃I in 2-propanol for 40s. Then, flow clean air over the substrate to dry. Next, spin coat the spiro-OMeTAD solution at 4000 rpm for 30s. Lastly, deposit 150 nm of Ag for the back contact under vacuum. All of these fabrication steps would be carried out in an N₂-purged glovebox, and the device would be stored in there as well. For testing, the final solar cell would have been illuminated under a solar simulator with an AM1.5G filter.

Power Converter Circuit

Solar panels produce a Direct Current (DC) voltage, however most

consumer appliances take an Alternating Current (AC) power input. Therefore, a power inverter is needed to convert the DC output from the solar panel into a standard 110 VAC 60 Hz output. We designed and simulated a power inverter using a Class D Half-Bridge topology, as shown in Figure 3.

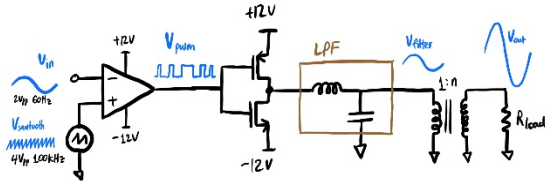


Figure 3. Schematic of Class D Half-Bridge inverter.

The Class D Half-Bridge inverter consists of a comparator that compares a reference 60 Hz sinusoidal signal with a high frequency sawtooth in order to produce a Pulse Width Modulated (PWM) square wave, which drives two switching transistors in order to deliver positive and negative charges from the DC input into an LC lowpass filter. The duty cycle of the PWM signal corresponds to the voltage of the output after the lowpass filter. Finally, the resulting low-voltage, high-current AC power is scaled to a high-voltage, low-current AC output using a transformer.

The main advantage of this topology is its simplicity. Driving the gate of the output stage transistors is very simple with just a single opamp. The inclusion of the transformer allows the switching transistors to handle lower voltages (albeit with higher current), so it is easy to drive their gates, and a high voltage DC rail is not needed.

A disadvantage of this topology is the requirement of both positive and negative DC rails. This requires the solar panels to be arranged into 2 groups in series such that each of the two groups produces 12V with approximately the same current output. This requirement can be eliminated

by using a Full-Bridge topology, which instead utilizes 4 switching transistors. However, the Full-Bridge converter would require a more sophisticated gate driver circuit.

Another disadvantage of this implementation is the usage of a P-channel MOSFET, which has half the carrier mobility of an equivalently sized N-channel device, as the high-side switching device. The P-channel device can be replaced with an N-channel device, but it would require a more complicated gate driver circuit.

References

- [1] N. Marinova, et. al. Organic and perovskite solar cells: Working principles, materials, and surfaces. *J. of Colloid and Interface Science* **488**, 373-389 (2017)
- [2] D. Liu and T. L. Kelly. Perovskite solar cells with a planar heterojunction structure prepared using room-temperature solution processing techniques. *Nature Photonics* **8**, 133-138 (2014).

Sous-Vide Simulation

Javier Corona, Aditi Munshi, Amlan Roy

Professor David Vallancourt

Electrical Engineering Department

Sous-vide technology enables slow-cooking of meats, vegetables, and more, evenly cooking the food and retaining maximum flavor. This is achieved by submerging a vacuum-sealed bag containing the food in a water bath, with temperature and cook time monitoring enabling precise cooking of the food. While use of the sous-vide began in the 1980s, its inhibitory cost prevented the technology from reaching home kitchens until the 2010s, when the price was reduced from thousands to a couple hundred dollars [1]. We explored different designs of the sous-vide through simulations, to better understand the technology and in turn make it more affordable. Due to COVID-19, we were unable to build a physical realization of this device as planned.

We first tore down an Instant Pot Accu Slim, priced at \$90, to understand how a major appliance company implements a sous vide. Figure 1 shows a complete circuit diagram for the Instant Pot. Despite the price point, the design was fairly simple. We found 3 heating elements, 2 temperature sensors, an LED driver and display, a buzzer, a DC motor, and a 32 KB microcontroller unit (MCU). This device's board consists largely of power regulation devices, controlled by the MCU. The MCU controls the current flow through the heating elements using an optocoupler, based on a feedback loop with the temperature sensors. While the water-reliance of the device prevented us from reading signals directly from the MCU, we deduced that it either uses pulse-width modulation (PWM) or on/off signals to control the current flow. The MCU also

monitored water level using capacitance, with the water acting as a dielectric. A capacitive system was implemented between the casings of the two temperature sensors, in parallel to another capacitor, in essence creating a capacitive current divider.

Our first simulation used a PWM control circuit without any use of an MCU. To simulate water heating, the circuit in Figure 2 was used, where temperature is analogous to voltage and heat flow to current. A capacitor emulates the heat capacity of water while behavioral current sources model heat flow in and out [2], with proportionality described by 3.00 W/K [3] and 1.16 W/K⁴ respectively. These were calculated using approximate container and heating element dimensions and a constant heat transfer coefficient. The results of the simulation can be seen in Figure 3.

Our second simulation combined a programmable logic controller (PLC), a resistance temperature detector (RTD), a Solid-State Relay (SSR), and a proportional integral derivative controller (PID). The RTD probe detects the temperature, which is then converted into a current output ranging from 4 to 20 mA. This signal is then fed back as PLC input, thus forming a feedback loop, and uses PWM to operate the SSR drive to regulate the power supply of the heating element.

References:

- [1] Cook's Illustrated (2018). The History of Sous Vide, Explained
- [2] Li, Shuhui & Chaloo, Rajab & McLauchlan, Robert. (2003). Heat Transfer Simulation Using PSpice
- [3] Engineering ToolBox, (2003). Overall Heat Transfer Coefficients for Fluids - Heat Exchanger Surface Combinations.

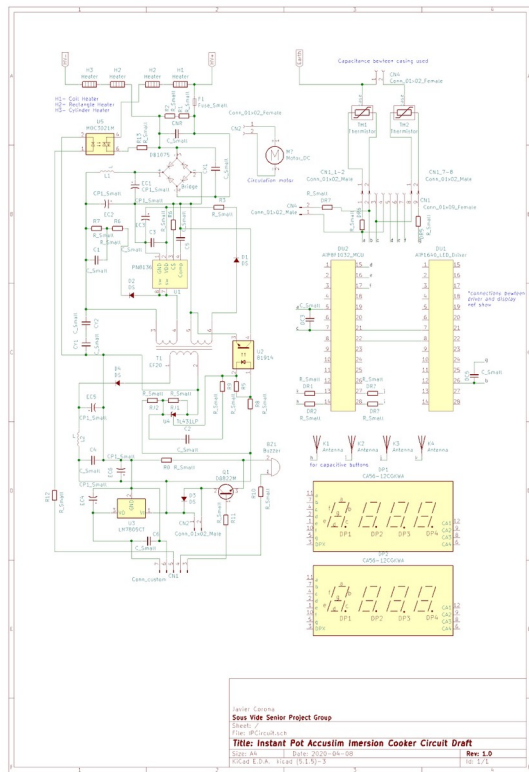


Figure 1. Instant Pot Circuit

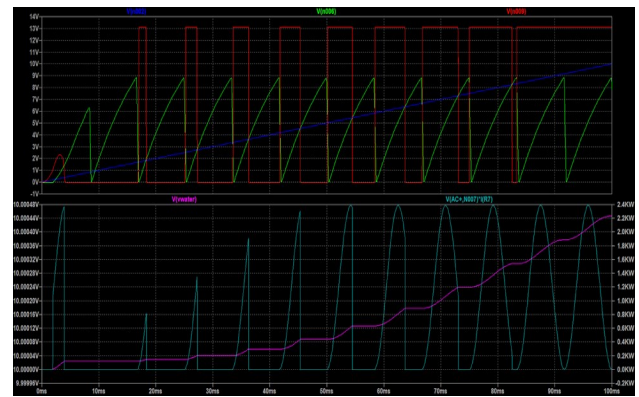


Figure 3. Results of Simulation. $V(n002)$ represents the temperature signal. $V(n004)$ is the ramp signal. $V(n004)$ is the resultant PWM signal. Below, we can see the power of the heating element and the temperature of the water, represented by V_{water} (with ambient temperature represented by 10V).

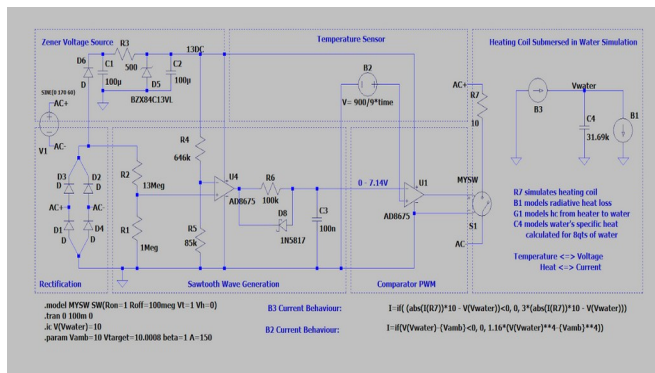


Figure 2. Simulation 1 Circuit Schematic

Theremin Project

Chuyun Liu

Prof. David Vallancourt, EE

The theremin is an electrical instrument that is played without contact. Developed about 100 years ago, one plays this instrument by controlling the distance of their hands from a volume and pitch antenna, which controls the volume and pitch of the instrument respectively. The project seeks to recreate the Theremin through only analog electrical components.

The Theremin consists of two main sub-circuits, one for pitch generation and another one for volume control. Oscillators are the core components of the Theremin, forming the basis of pitch generation and volume control. The design uses four oscillators, two for the pitch generation circuit and two for the volume control circuit. LC oscillators are used for both pitch and volume circuits to allow the frequency of oscillation to change in accordance to the capacitance changes from movement of the player's hand around the antennas.

For the pitch sub-circuit, the LC oscillator's frequency of oscillation is set to 260 kHz, far above the audible range. To lower the frequency to the audible range, the signal of the LC output oscillator is multiplied using a prebuilt integrated circuit with the output of a Wien bridge oscillator and then passed through a 7th order Chebyshev II filter low-pass filter. The LPF removes the higher frequency component of the output signal, leaving a signal that can be heard by ear once it is converted to sound.

In the volume control sub-circuit, the signal from the LC volume oscillator set to 260 kHz is multiplied with the signal from another oscillator and filtered such that the output signal is around the 10 kHz. The signal is then converted a square wave of the same frequency using a Schmitt trigger.

To control volume using frequency, the output of the Schmitt trigger is passed through an IC frequency-to-voltage converter. The output of the f-to-v circuit is then connected to a variable gain amplifier which amplifies the signal from the pitch circuit. The VCA circuit is what ties together the pitch and volume portion of the circuit.

In this arrangement, a change in frequency will corresponds to a change in voltage and subsequently the gain of the VCA circuit. This will allow the Theremin audio signal to be amplified according to the distance of the player's hands from the pitch antenna.

Figure 1: Full Block Diagram

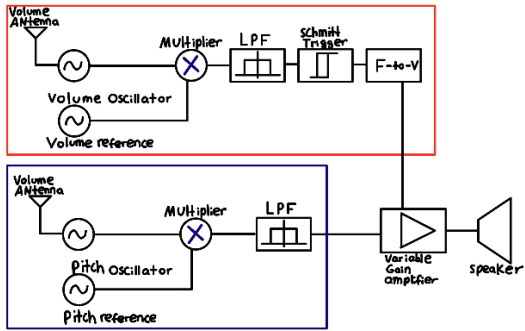


Figure 2: Implementation of Pitch Generation

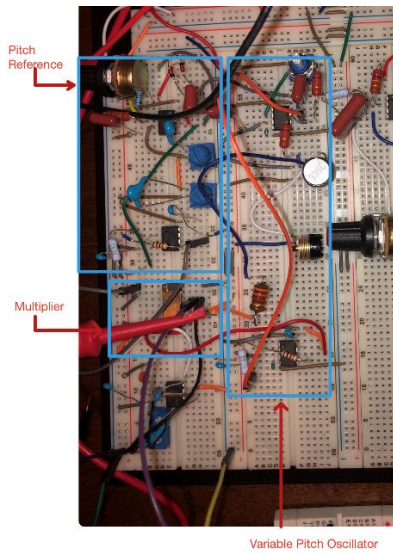


Figure 3: Low Pass Filter

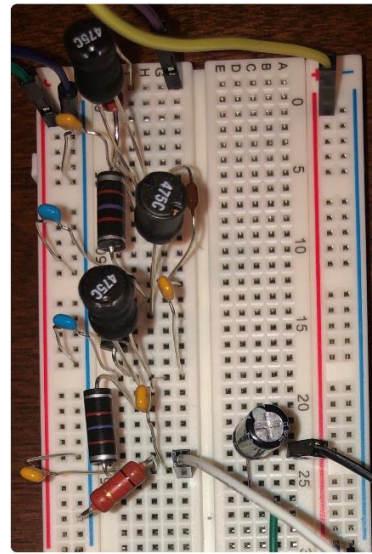
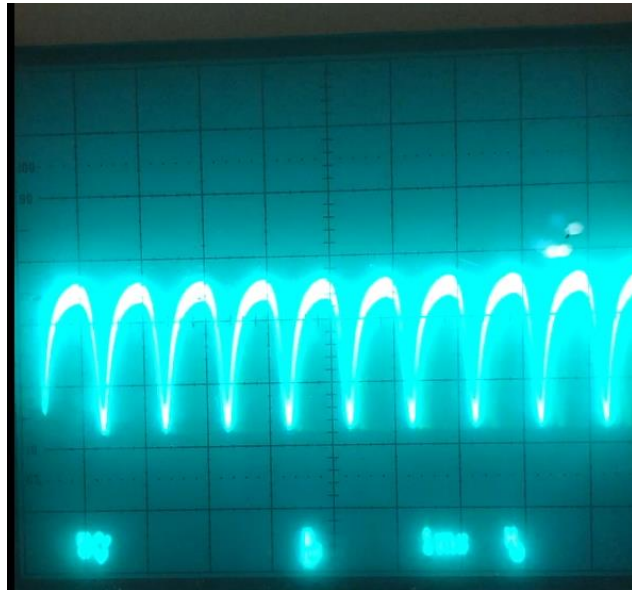


Figure 4: Setup



Figure 5: Output



STALLION: Video Adaptation Algorithm for Low-Latency Video Streaming

Craig Gutterman[†], Brayn Fridman[‡], Trey Gilliland[†], Yusheng Hu, Gil Zussman[†]

[†]Electrical Engineering, Columbia University,

ABSTRACT

As video traffic dominates the Internet, there has been an increased interest in near-second low-latency streaming. Prior low-latency streaming platforms rely on using tens of seconds of video in the buffer to offer a seamless experience. Striving for near-second latency requires the receiver to make quick decisions regarding the download bitrate and the playback speed. To alleviate these issues, we design a new adaptive bitrate (ABR) scheme, *Stallion*, for **STANDARD Low-LATency vIdEO cONTrol**. *Stallion* uses a sliding window to measure the mean and standard deviation of both the bandwidth and latency. The ABR algorithm is evaluated against the standard DASH DYNAMIC algorithm over a variety of networking conditions. *Stallion* shows 1.75x increase in bitrate, and 5x reduction in the number of stalls.

ACM Reference Format:

Craig Gutterman[†], Brayn Fridman[‡], Trey Gilliland[†], Yusheng Hu, Gil Zussman[†]. 2020. STALLION: Video Adaptation Algorithm for Low-Latency Video Streaming. In *Proceedings of ACM Multimedia Systems Conference (MMSys'20)*. ACM, New York, NY, USA, 6 pages. https://doi.org/10.475/123_4

1 INTRODUCTION

Video has dominated Internet traffic in recent years. Recently there has been an increased usage of live video streaming, and it is expected to grow to 13% of total internet traffic by 2021 [3]. To offer clients a high quality of experience it is essential for live streams to minimize the video streaming latency. On-demand streaming services usually rely on tens of seconds of video to be stored on the client buffer. This gives the service time to adapt to changes in network conditions while still offering a good quality of experience (QoE). On the contrary, live streaming requires much lower latency, resulting in a reduced buffer on the client device. The service needs to adapt quickly to network changes while also offering a high video resolution and minimize the amount of stall events.

A majority of streaming services rely on HTTP Adaptive Streaming (HAS) to deliver video over the Internet. One of the most popular techniques is Dynamic Adaptive Streaming over HTTP (DASH) or MPEG-DASH [31], [36]. For HAS each video is divided into

shorter segments of video (usually a few seconds of video). Each of the segments is encoded in multiple resolutions and bitrates. The clients use a bitrate adaption (ABR) to dynamically request segments to maximize the user QoE. DASH ABR algorithms are either buffer-based (e.g., BOLA [17]), throughput-based (e.g., OBOE [5]) or hybrid (e.g., DYNAMIC [16]). One of the main issues with these algorithms is that they are not designed to work for low-latency streaming.

Given this challenge, our objective is to design an ABR algorithm for near-second latency. We present *Stallion*, for **STANDARD Low-LATency vIdEO cONTrol**. *Stallion* uses a sliding window to measure the mean and standard deviation of both the bandwidth and latency. Prior algorithms incorporated into DASH only rely on using the buffer level as well as the mean (either sliding window or expected weighted moving average (EWMA)) of throughput and latency. To deal with variable network conditions near-second streaming requires additional information about the variations in the throughput and latency on a per segment basis. Therefore we design a system a throughput-based state that incorporates the standard deviation of these throughput and latency. This to increase the average bitrate as well as reducing the amount of stalls.

We implement *Stallion* in the modified dash.js reference player provided by the ACM MMSys Grand Challenge [1]. This player is modified from the standard dash player [4] to pre-request low latency segments. This enables the player to request the segment before they are available on the server.

To examine the performance of *Stallion* we tested *Stallion* against DYNAMIC [16] with the 5 network profiles provided by [1]. Our results show that *Stallion* outperforms DYNAMIC. In particular, it achieves higher QoE with a 1.75x increase in bitrate, and 5x reduction in the number of stalls. The code for *Stallion* is available for testing by the reviewers [?].

The rest of the paper is organized as follows. Section 2 provides background on ABR algorithms. Section 3 presents our preliminary findings on low-latency streaming. It then continues to describe the system and implementation of *Stallion*. Section 4 describes our experimental setup. It then continues with the QoE evaluation and the network traces used for evaluation. In addition, we discuss the performance results of *Stallion* vs. DYNAMIC. Section 5 concludes and discusses future directions.

2 BACKGROUND AND RELATED WORK

HTTP Adaptive Streaming (HAS) is being used by majority of streaming services to deliver video over the internet. One of the most common formats is Dynamic Adaptive Streaming over HTTP (DASH) or MPEG-DASH [18, 19].

HAS encodes a video in multiple resolutions and bitrates. Each encoding is then divided into a number of *segments* of variable

Permission to make digital or hard copies of part or all of this work for personal or classroom use is granted without fee provided that copies are not made or distributed for profit or commercial advantage and that copies bear this notice and the full citation on the first page. Copyrights for third-party components of this work must be honored. For all other uses, contact the owner/author(s).

MMSys'20, June 2020, Amherst, MA, USA

© 2020 Copyright held by the owner/author(s).

ACM ISBN 123-4567-24-567/08/06...\$15.00

https://doi.org/10.475/123_4

length (usually a few seconds of video) [12]. Clips are either encoded with Variable Bitrate (VBR) encoding or with Constant Bitrate (CBR).

Details that the client can download from local servers are given in a DASH Media Presentation Description (MPD) file. For each segment request, an HTTP GET request is sent to the server. The GET request is followed by a response of downloading the requested segment. This allows the video player of the client to dynamically request segments based on the ABR algorithm. The client contains a client buffer to temporarily store segments of the video. This is used to ensure a smooth playback. When there are no segments stored in the buffer it results in a playback stall event.

While a majority of services use HAS, each has its own method of ABR streaming [12]. ABR requires either TCP or any other reliable transport [8] and is usually delivered over HTTP(S). The ABR algorithms rely on statistics such as throughput, buffer health, or are hybrid (throughput and buffer) to determine the optimal segment to request. Thus, the player can switch to a segment with a lower bitrate when the estimated bandwidth or buffer is low to avoid stalling. If the bandwidth becomes available at a future time, the player can switch back to a higher bitrate to provide a greater user experience.

We give further details about the different types of ABR algorithms.

Buffered-based: Buffer-based ABR algorithms rely on using the buffer level to determine the optimal bitrate of the requested segment. BOLA [17] is an ABR algorithm that determines that bitrate from buffer occupancy. As the buffer occupancy grows, higher bitrate segments are preferred. One drawback of BOLA is that it usually performs better with higher buffer levels [16]. [9] selects the bitrate with the goal of minimizing stalls and keeping the buffer occupancy level about a certain threshold. When the level exceeds 15 sec, it switches to the highest available bitrate.

Throughput-based: Throughput-based ABR algorithms collect and calculate all the transmission information between the server and the client to estimate the available throughput. The estimated throughput is then used to determine the optimal bitrate for the next video segment. Oboe [5] aims to ensure good user QoE by enabling auto tuning configuration parameters of the ABR algorithm based on the current network state. Additional throughput-based algorithms include FESTIVE [10], and PANDA [11].

Hybrid-based: Hybrid-based ABR algorithms implement both buffer-based and throughput-based algorithms. DYNAMIC [16] is a hybrid algorithm that is built into the official DASH reference player. It uses a version of BOLA for its buffer-based algorithm (when the buffer is high) as well as a throughput rule for its throughput-based algorithm (when the buffer is low or empty). Additional hybrid based algorithms include ELASTIC [7], and MPC [20]. Penseive [13] utilized reinforcement learning for generating optimal ABR algorithms. The neural network model is based on the data from client players. Penseive gradually learns to make better ABR decisions through reinforcement in the form of reward signals that reflect video QoE for past decisions. HotDASH [15] also uses reinforcement learning for its decision engine as well as prefetching of video segments.

Recently there has been additional research for ABR algorithms specifically designed to deal with low-latency streaming. LOLY-POP [14] is designed for low-delay video streaming and uses TCP throughput predictions on times scales of 1 to 10 sec. ACTE [6] using a sliding window to estimate bandwidth and uses a linear adaptive filter to predict future bandwidth.

3 STALLION SYSTEM DESIGN

In this section, we first describe our preliminary observations of DYNAMIC in the dash.js reference player modified to pre-request low latency segments. The segment size is set to be 0.5 sec. We then develop *Stallion*, a throughput-based ABR algorithm to work effectively in low-latency settings with variable network conditions.

3.1 Preliminary Low-Latency DASH Findings

To determine the best way to improve the performance of DASH we initially run experiments using the default Hybrid ABR algorithms in DASH. This controller contains a collection of ABR rules including ThroughputRule, BolaRule, InsufficientBufferRule, SwitchHistoryRule, and DroppedFramesRule. The hybrid model dynamically chooses either the BOLA or Throughput rule depending on the buffer level. The three remaining rules are also used to offer an option of quality requested. The minimum of the 4 qualities is the final chosen quality.

The Hybrid ABR algorithms network settings described in Section 2, are used to test the initial performance. One of the preliminary findings is that because the buffer is low, throughput rule is usually chosen instead of BOLA. In addition, the ultimate decision was usually the result of the insufficient buffer rule being chosen.

Even with the low buffer rule being chosen there were frequent stalls as there was not sufficient time to adjust to changes in the network conditions. The stalls led to an increase in the live playback latency. In an effort to minimize this the playback controller increases the playback rate, resulting in additional stalls.

3.2 Stallion Implementation

The observations in 3.2 influenced the design of Stallion. Fig 1(a) shows the system design of *Stallion* in the dash.js reference player modified to pre-request low latency segments along with the system added to log results [1].

The constraints that were given were that the segment duration, the segment chunk size, and the prerequest behavior could not be changed. Beyond the design of a custom rule Stallion.js, we modified additional functionality of ThroughputHistory.js, PlaybackController.js, AbrController.js, and index.html. The resulting ABR system for *Stallion* is represented in Fig. 1(b). In addition, to the *Stallion* rule, we use the Switch History and Dropped Frame rules in DYNAMIC.

The first parameter that needs to be initially set is the target latency of ABR algorithm. The initial setting of target latency of the near-second low latency DASH player is 1 sec. This means that after 1 segment (0.5 sec) of playback, the next segment should be sent to the client. This means that the next segment needs to be downloaded before the current one is playing otherwise a stall will occur. This gives a minimal amount of time to deal with any unstable

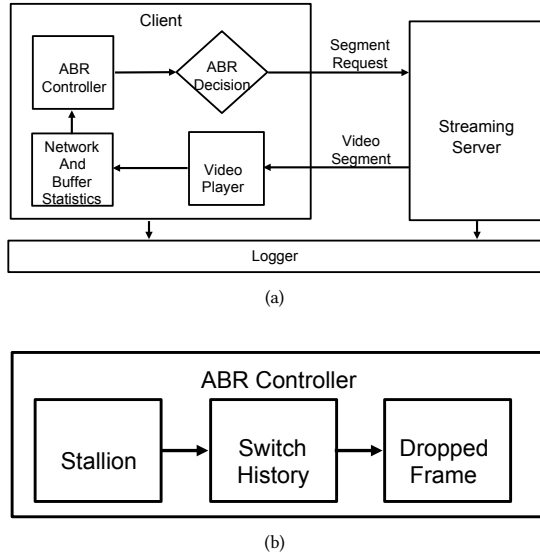


Figure 1: (a) The dash.js player with additional modifications to switch ABR algorithm and log results, (b) Stallion ABR controller.

network conditions. Therefore we update the initial target latency of the DASH player to 1.5 sec. This leaves 1 additional segment in the buffer of the client and additional time for the DASH player to adapt to network conditions.

One of the major prior issues of playback was the playback rate of the video. When the playback falls behind the target latency, the controller attempts to catch up the the target latency by increasing the playback rate. This occurs even when the buffer is low (but not completely stalled). Increasing the playback rate when the buffer is low would likely only increase the amount of stalls, thereby increasing the latency further. We make the following modification to improve the performance for low latency. If the player has a latency greater than the target latency, it will only increase the playback rate if the buffer level is greater than 0.6 sec.

We develop a custom throughput-based rule, *Stallion*, that is used to estimate a safe throughput and latency for near-second low-latency streaming. Unstable network conditions result in client bandwidth fluctuations during playback. Relying only on the mean of the throughput and latency leaves out details in the statistics of the network pattern that can be beneficial when determining the optimal video segment to request. Therefore, *Stallion* relies on the use of the standard deviations of both latency and throughput to make a safe estimate for our quality prediction.

The throughput, Thr^s , of sample s is measured by taking the download size and dividing it by the download time. Each latency sample, L^s is measured by the time the request is sent to the time the first packet of the segment is delivered. The first data points needed are the average throughput, \bar{Thr}_n , and the average latency, \bar{L}_n . These metrics are already built in ThroughputHistory.js. The sliding window sample mean is calculated over a maximum of $n = 20$ samples.

In addition, we add methods to ThroughputHistory.js to calculate the sample standard deviation of both the throughput and latency for the sliding window. The sample standard deviation of the throughput is represented as σ_n^{Thr} . The sample standard deviation of the latency is represented as σ_n^L . These data points are used to assign safe estimates for the bitrate and latency. Accordingly, we set:

$$\hat{Bitrate} = \bar{Thr}_n - z_{Thr} \sigma_n^{Thr}$$

$$\hat{Latency} = \bar{L}_n + z_L \sigma_n^L$$

These two estimates are then inputted to `abrController.getQualityForBitrate()` to determine the highest possible segment quality that can be requested given the constraints of $\hat{Bitrate}$ and $\hat{Latency}$. The goal of this function is determine what is the maximal quality of the next segment that can be delivered during a segment duration. The latency is subtracted from the fragment duration to determine the dead time. The remaining time is the amount of time during the segment duration that can be used to download. This time is then multiplied with $\hat{Bitrate}$, to determine the actual realizable bitrate. The segment with the highest bitrate less than the realizable bitrate is the bitrate chosen by *Stallion*.

4 EVALUATION

We develop a testing and logging framework to measure the performance of the proposed ABR algorithm vs. a baseline system. The testing of the algorithms are done by using a variety of network profiles with unstable network conditions. We then describe the relevant metrics used for evaluation along with the calculation of the QoE metric. We then use these components to evaluate the performance of *Stallion* vs. DYNAMIC.

4.1 Experimental Setup

As ABR streaming is comprised of many components working together to optimize playback quality, each component relies on observations about the current network conditions available to the client. To measure the performance and provide us with feedback on how ABR modifications impact the playback experience, we write various metrics throughout the framework to a log file. With this log file, we measure the performance of each ABR algorithm on the playback quality. The testing script runs through multiple runs of each network trace. Further details about the network traces are described in Sec. ??.

To sufficiently test our modifications, we develop an automated script to run through multiple tests of our modified player on each network testing profile. This script saves the test log file and results JSON from each individual test which are then used to measure the performance throughout the entire experiment. T

The video used for testing is Big Buck Bunny [2]. Each video is encoded in 3 bitrates of 200 Kbps, 600 kbps, and 1000 kbps. The associated video qualities of these bitrates are 360p, 480p, and 720p, respectively.

All experiments were conducted on a Macbook Pro laptop with a 2.8 GhZ Intel Core I7 with 16 GB of RAM. Both the server and

Table 1: Network Profiles

Notation	Time Duration (sec)	Speed (Kbps)
Cascade	(30,30,30,30,30)	(1200,800,400,800,1200)
Intra Cascade	(15,15,15,15,15,15,15,15)	(100,800,600,400,200,400,600,800,1000)
Spike	(10,10,10)	(1200,300,800)
Slow Jitters	(5,5,5,5,5,5)	(500,1200,500,1200,500,1200)
Fast Jitters	(0.25,5,0.1,1,0.25,5)	(500,1200,500,1200,500,1200)

the dash player were run on the laptop. The dash.js player ran in Google Chrome browser.

4.2 Network Traces

There are 5 network profiles which are used for testing. The details of the 5 networking patterns can be seen in Table 1. Each network profile has a network pattern that is repeated twice per experiment.

The first network profile is Cascade. This pattern lasts for roughly 150 seconds with 30 second intervals at network speeds of 1200 Kbps, 800 Kbps, 400 Kbps, 800 Kbps, and back to 1200 Kbps. The second network profile is Intra Cascade. This profile contains a pattern with 9 steps of 200 Kbps for 15 seconds each. The steps begin at 1000 Kbps going down to 200 Kbps, and then back up to 1000 Kbps. The third profile is labeled as Spike. This profile has 3 steps lasting 10 sec each: 1200 Kbps, 300 Kbps, and 800 Kbps. The fourth profile has a pattern that is 30 seconds and switches between 500 Kbps and 1200 Kbps every 5 sec. The fifth profile tested is Fast Jitters, with a network pattern of 11.6 seconds. The speeds of this profile are 500 Kbps, 1200 Kbps, 500 Kbps, 1200 Kbps, 500 Kbps, and 1200 Kbps with durations of 0.25 sec, 5 sec, 0.1 sec, 1 sec, 0.25 sec, and 5 sec, respectively.

4.3 QoE Model

We focus on 5 metrics for our evaluation criteria. The first criteria is the average selected bitrate (Kbps). The second metric is average live latency. The live latency is measured as the amount of time between when the original video was 'created' until it is played back. The third criteria is the average number of bitrate switches. While higher bitrates are in general better for the quality of experience of the user, bitrate switches have negative impact on the user's viewing experience. The fifth metric is stall duration. The longer the stall duration the higher the negative impact on the user's experience.

The quality of experience model used for evaluation is based on the document provided by [https://github.com/twitchtv/acm-mmsys-2020-grand-challenge/blob/master/NQoE.pdf]. We use the per-segment QoE for evaluation. For the low latency model, segment duration is 0.5 sec. List of notations for QoE function can be found in Table ?. Overall the QoE model is calculated as:

$$QoE = \sum_{s=1}^S (\alpha R_s - \beta E_s - \gamma L_s - \sigma |1 - P_s|) - \sum_{s=1}^{S-1} \mu |R_{s+1} - R_s|$$

To make all the rewards on the same scale we set the reward for specific bitrates as:

$$R_s = \log_{10}\left(\frac{\text{Bitrate (Kbps)}}{100Kbps}\right)$$

Table 2: List of notations for QoE function

Notation	Meaning
s	A segment
R_s	Reward of Segment bitrate (Kbps)
E	REbuffering time (seconds)
L	Live latency (seconds)
P	Playback Speed
S	Total number of segments
α	Bitrate reward factor (0.5 sec)
β	Rebuffering penalty factor (= R_s for 1000 Kbps)
γ	Live Latency penalty factor (if $L \leq 1.1$ sec then = 0.005, otherwise = 0.01)
σ	Playback speed penalty factor (= R_s for 200 Kbps)
μ	Bitrate switch penalty factor (0.02 sec)

4.4 Results

We evaluate the performance of *Stallion* against the low-latency ABR algorithm using the Dynamic ABR algorithm. We tune the parameters of z_{Thr} and z_L to optimize the performance of *Stallion*. The final rule tested in the paper has z_{Thr} set to 1 and z_L set to 1.25. Each ABR algorithm was run 20 times on each network profile. Fig. 2 shows the results of these tests. For each box plot, the middle red line is the median value. The bottom of the box represents Q1 (25-percentile) and the top of the box represents Q3 (75-percentile) of the dataset respectively. The lower extended line represents Q1-1.5IQR, where IQR is the inner quartile range (Q3-Q1). The higher extended line represents Q3 + 1.5IQR. We further discuss the results for each QoE metric and the total QoE as follows:

Bitrate: One of the primary objectives of an ABR algorithm is to maximize the bitrate of the video playing. For all 5 network profiles Dynamic has a median bitrate less than 300 Kbps. The median bitrate for *Stallion* is greater for every network profile tested. In 4 of the 5 profiles there was atleast a 200 Kbps increase in average bitrate. Overall the average bitrate increased from 300 Kbps to 520 Kbps, a 1.75x increase in average bitrate.

Average live latency: For Dynamic the target latency is set to 1 sec, while it is set to 1.5 for *Stallion*. The average live latency for Dynamic is less than 1.5 sec in all network profiles except intra. For *Stallion*, the worst performing network profile is spike. For spike the average live latency is at 2 sec, while the rest of the network profiles are slightly above 1.5 sec.

Number of playback rate switches: We analyze the stability of the playback based on the number of playback rate switches. The performance for both ABR algorithms tested is comparable for all network profiles. Each ABR algorithm has a median number of switches less than 10 for each network profile.

Absolute Playback Error: The absolute playback error for each segment is calculated as $|1 - P_s|$. The absolute playback error is calculated as the sum of the playback error for each video segment of an experiment. Both *Stallion* and Dynamic perform well for fast jitters and playback rate is kept constant at 1. For *Stallion* the absolute playback error is kept below 5 for all experiments. Dynamic performs considerably worse in network patterns of cascade and intra.

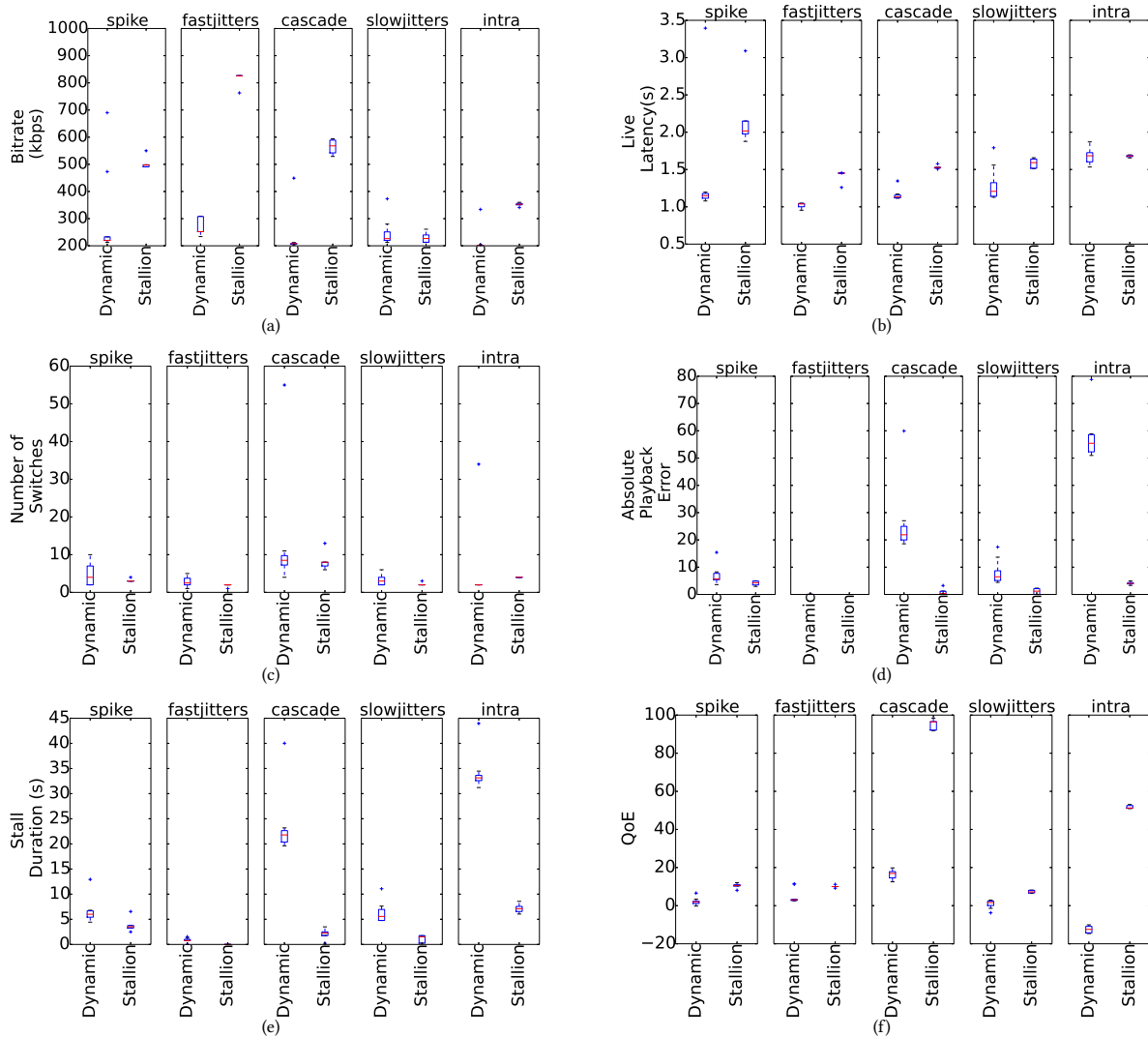


Figure 2: Performance comparison of Dynamic and Stallion for each network pattern: (a) Average bitrate, (b) Average live latency, (c) Number of playback rate switches, (d) Absolute Playback Error, (e) Stall Duration (s), (f) QoE. For each box plot, the middle red line is the median value. The bottom of the box represents Q1 (25-percentile) and the top of the box represents Q3 (75-percentile) of the dataset respectively. The lower extended line represents Q1-1.5IQR, where IQR is the inner quartile range (Q3-Q1). The higher extended line represents Q3 + 1.5IQR.

Stall Duration: One of the main issues that can occur during near-second low-latency is the number of stall durations and the amount of time with the video stalled. For spike network pattern Dynamic has a median of 6 sec of stall duration while *Stallion* has a median of 3 sec. For fast jitters both perform well with less than 1 second of stall duration. For cascade there is a large improvement in stall duration as Dynamic has a median of 22 seconds while *Stallion* has a median of 3 seconds. For the slow jitters network profile Dynamic has a stall duration of 6 sec, while *Stallion* has a stall duration of 2 sec. Dynamic performs the worse for the intra network profile. It has a median stall duration of 33 sec. This network profile is also the worst for *Stallion* with a median stall duration of 7 sec. Overall the average stall duration of *Stallion* is 2.8 sec, compared

to an average stall duration of 14.3 sec. This is 5x improvement in stall duration for *Stallion*.

QoE: The QoE score is calculated based on the details given in 4.3 and Table 2. The weights given can be adapted depending on the objectives. *Stallion* outperformed the QoE in all network profiles. The profiles that saw the biggest improvement were cascade and intra.

Overall, *Stallion* can be shown to have improved QoE for near-second low latency streaming. *Stallion* had better performance in 4 of the 5 key QoE metrics, with the exception of an increased live latency. The design of *Stallion* to use the information given by the second order standard deviation in the latency and bitrate estimates gave it the ability to make safer decisions. These safer

decisions allowed *Stallion* to not only reduce the amount of stalls considerably but also improve the bitrate without increasing the amount of bitrate changes.

5 CONCLUSION

We present *Stallion*, an ABR scheme designed for near-second low-latency video control. The metric relies on (i) a segment based sliding window of the bitrate and latency of previous segments, and (ii) the mean and standard deviation of this window to estimate the bitrate and latency available for the next segment. We determine that specifically with a near-second target latency the additional information from the window gives a better estimate of the available bandwidth.

Stallion is evaluated against DASH standard DYNAMIC over a variety of networking conditions. On average *Stallion* shows 1.75 increase in bitrate, and a 5x reduction in the number of stalls.

For future research we would like to add additional network profiles and use a machine learning based system that auto adapts the tuning parameters of *Stallion* during video playback.

REFERENCES

- [1] acm-mmsys-2020-grand-challenge. <https://github.com/twitchtv/acm-mmsys-2020-grand-challenge>.
- [2] Big buck bunny. <https://peach.blender.org/>.
- [3] Cable live video usage will increase 15-fold by 2021, cisco predicts. <https://www.fiercevideo.com/cable/live-video-usage-will-increase-15-fold-by-2021-cisco-predicts>.
- [4] Dash industry forum (dash-if). <https://reference.dashif.org/dash.js/v3.0.3/samples/dash-if-reference-player/index.html>.
- [5] Z. Akhtar, Y. S. Nam, R. Govindan, S. Rao, J. Chen, E. Katz-Bassett, B. Ribeiro, J. Zhan, and H. Zhang. Oboe: auto-tuning video abr algorithms to network conditions. In *Proceedings of the 2018 Conference of the ACM Special Interest Group on Data Communication*, pages 44–58, 2018.
- [6] A. Bentaleb, C. Timmerer, A. C. Begen, and R. Zimmermann. Bandwidth prediction in low-latency chunked streaming. In *Proceedings of the 29th ACM Workshop on Network and Operating Systems Support for Digital Audio and Video*, pages 7–13, 2019.
- [7] L. De Cicco, V. Caldaralo, V. Palmisano, and S. Mascolo. Elastic: a client-side controller for dynamic adaptive streaming over http (dash). In *2013 20th International Packet Video Workshop*, pages 1–8. IEEE, 2013.
- [8] R. T. Fielding and J. F. Reschke. Hypertext transfer protocol (HTTP/1.1): message syntax and routing. *RFC*, 7230:1–89, 2014.
- [9] T.-Y. Huang, R. Johari, N. McKeown, M. Trunnell, and M. Watson. A buffer-based approach to rate adaptation: Evidence from a large video streaming service. In *Proceedings of the 2014 ACM conference on SIGCOMM*, pages 187–198, 2014.
- [10] J. Jiang, V. Sekar, and H. Zhang. Improving fairness, efficiency, and stability in http-based adaptive video streaming with festive. In *Proceedings of the 8th international conference on Emerging networking experiments and technologies*, pages 97–108, 2012.
- [11] Z. Li, X. Zhu, J. Gahn, R. Pan, H. Hu, A. C. Begen, and D. Oran. Probe and adapt: Rate adaptation for http video streaming at scale. *IEEE Journal on Selected Areas in Communications*, 32(4):719–733, 2014.
- [12] A. Mansy, M. H. Ammar, J. Chandrashekar, and A. Sheth. Characterizing client behavior of commercial mobile video streaming services. In *Proc. ACM MoVid*, Mar. 2014.
- [13] H. Mao, R. Netravali, and M. Alizadeh. Neural adaptive video streaming with pensieve. In *Proceedings of the Conference of the ACM Special Interest Group on Data Communication*, pages 197–210, 2017.
- [14] K. Miller, A.-K. Al-Tamimi, and A. Wolisz. Qoe-based low-delay live streaming using throughput predictions. *ACM Transactions on Multimedia Computing, Communications, and Applications (TOMM)*, 13(1):1–24, 2016.
- [15] S. Sengupta, N. Ganguly, S. Chakraborty, and P. De. Hotdash: Hotspot aware adaptive video streaming using deep reinforcement learning. In *2018 IEEE 26th International Conference on Network Protocols (ICNP)*, pages 165–175. IEEE, 2018.
- [16] K. Spiteri, R. Sitaraman, and D. Sparacio. From theory to practice: Improving bitrate adaptation in the dash reference player. *ACM Transactions on Multimedia Computing, Communications, and Applications (TOMM)*, 15(2s):1–29, 2019.
- [17] K. Spiteri, R. Uргаonkar, and R. K. Sitaraman. Bola: Near-optimal bitrate adaptation for online videos. In *IEEE INFOCOM 2016-The 35th Annual IEEE International Conference on Computer Communications*, pages 1–9. IEEE, 2016.
- [18] T. Stockhammer. Dynamic adaptive streaming over HTTP -: standards and design principles. In *Proc. ACM MMSys*, Feb. 2011.
- [19] N. Weil. The state of MPEG-DASH 2016. <http://www.streamingmedia.com/Articles/Articles/Editorial/Featured-Articles/The-State-of-MPEG-DASH-2016-110099.aspx>.
- [20] X. Yin, A. Jindal, V. Sekar, and B. Sinopoli. A control-theoretic approach for dynamic adaptive video streaming over http. In *Proceedings of the 2015 ACM Conference on Special Interest Group on Data Communication*, pages 325–338, 2015.

EE Senior Design Project Proceedings

Virtual Projection Notepad

Jason “Tianyi” Dai (td2593), Austin Ebel (abe2122), Zhenguo “Brian” Wu (zw2542)¹

The design of an optical virtual keyboard, which optically detects and analyzes finger motions, has been around since the early 1990s. It offers the possibility of replacing rigid mechanical inputs with physically virtual inputs and has the potential to optimize for specific applications such as classroom note-taking, gaming and drawing. In addition to keyboards, other inputs such as writing/drawing pads offer the same merits and functionalities but are less developed. Therefore, we designed an architecture for projected virtual writing/drawing pad whereby the image of a virtual screen is projected onto a surface: when a user draws on the surface, the device records the corresponding strokes and registers as device inputs that could be then converted to texts or drawings.

The current version of the device is designed to embed on a BeagleBone Black (BBB) with Debian/Linux operating system. The projection of the screen is done using a DLP Lightcrafter 2000 which connects to the BBB. In order to magnify the image projected at an appropriate device length (approx. 25 cm), the screen image is designed to be projected vertically upward to a 99% reflective aluminum mirror (approx. 25 cm above) which then redirects the projected beams onto the surface at a larger scale. The distance and angle of the mirror is adjusted alongside with the output image of the projector to achieve a clear and non-distorted image projection, although some resolution and intensity are necessarily compromised in the reflection process. The output of the Lightcrafter is a GUI designed using PyQt5 which includes a main canvas, a write/paint tool selection panel and a color selection panel, similar to the well known app Paint. The work flow of the system is shown in Figure.1.

The device requires an IR pen which can be simply put together using an IR LED (860 nm) with 4 AAAA batteries (Fig. 3). A long pass filter with cutoff frequency at 696 nm is attached in front of the USB camera lens connected to the BBB. This way, all visible light going into the camera lens is filtered out, leaving the image

completely dark except for the one point lit up by the IR LED moving in the field of view of the lens. The schematic architecture of the device is shown in Fig.2. The outer structure of the device is designed to be a foldable 3D printed case so that the storage of the device can be more compact.

A Gaussian smoothing algorithm is applied to the IR filtered video feed to remove additional noise, and the brightest pixel is extracted from each frame to serve as the true position of the IR pen. This, in conjunction with a mapping between pixel coordinates in the frame and positions in our UI allows for the recreation of what is being drawn with the IR pen on the UI, and ultimately projected back to the user through the DLP projector. Once a word or phrase has been drawn, the user can optionally perform handwritten text recognition through a pre-trained neural network on the IAM dataset. The model itself takes in a 128x32 gray-scale image, passes it through five convolutional layers, then through two LSTM layers, and finally to the output for a classification accuracy of 74%. Once converted, the user can save the output as an image or PDF, making this tool perfect for note-taking without the need for an expensive tablet, as writing can be done on any surface imaginable.

The portability and compactness of our device allow its users to easily interact with the software interface using hand gestures and handwriting to considerably simplify the control for embedded systems. Multiple User Interfaces (UIs) were developed as part of our software component to provide versatile device functionalities. For instance, our prototype is aimed at being programmed to switch between usage scenarios to support the UI of a writing/drawing notebook or a remote control (not currently implemented but is a potential extension). The proposed interface architecture can fundamentally change the way people interact with the ubiquitous IoT devices in the future.

¹This work was supported by the Electrical Engineering Department at Columbia University in the City of New York

I. DIAGRAMS

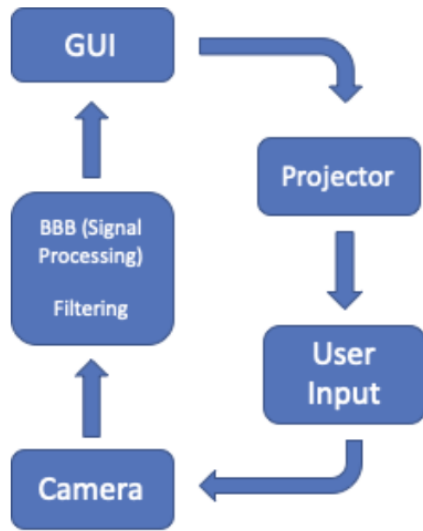


Fig. 1: Block diagram the virtual projection system.

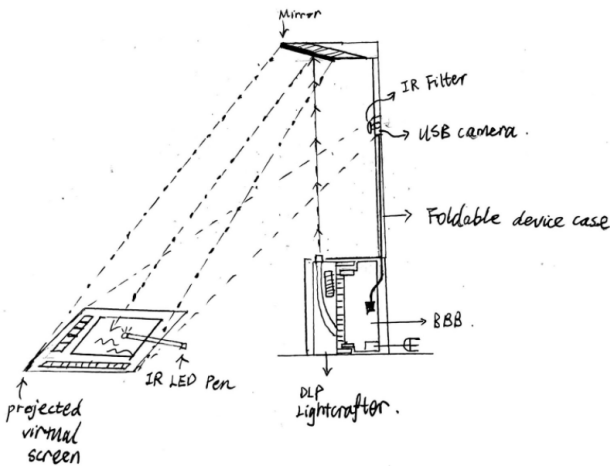


Fig. 2: Mechanical structure schematic of the system.

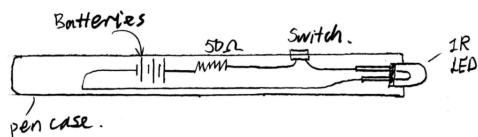


Fig. 3: Circuit schematic for the IR LED pen.

REFERENCES

- [1] Coley, Gerald. "Beaglebone black system reference manual." Texas Instruments, Dallas 5 (2013).
- [2] Instruments, Texas. "DLP LightCrafter Evaluation Module." (2014).
- [3] Jo, D., & Kim, G. J. (2019). AR Enabled IoT for a Smart and Interactive Environment: A Survey and Future Directions. Sensors (Basel, Switzerland), 19(19), 4330.
- [4] Jung, Timothy; Claudia Tom Dieck, M. (4 September 2017). Augmented reality and virtual reality : empowering human, place and business. Jung, Timothy,, Dieck, M. Claudia tom. Cham, Switzerland.
- [5] Rouchouze, Bruno. "Projected and secured virtual keyboard." U.S. Patent No. 8,624,842. 7 Jan. 2014.
- [6] Wijewantha, Nadeeka Samantha, and Chanaka Amarasekara. "VistaKey: A Keyboard Without A Keyboard—A Type Of Virtual Keyboard." Final year project thesis, Informatics Institute of Technology, Wellawatta, Sri Lanka (2004)
- [7] Y. Sun, A. Armengol-Urpi, S. N. Reddy Kantareddy, J. Siegel and S. Sarma, "MagicHand: Interact with IoT Devices in Augmented Reality Environment," 2019 IEEE Conference on Virtual Reality and 3D User Interfaces (VR), Osaka, Japan, 2019, pp. 1738-1743.
- [8] <https://github.com/githubharald/SimpleHTR>
- [9] <https://github.com/learnpyqt/15-minute-apps/tree/master/paint>
- [10] "IAM Handwriting Database." IAM Handwriting Database - Computer Vision and Artificial Intelligence, www.fki.inf.unibe.ch/databases/iam-handwriting-database.

MECHANICAL ENGINEERING

InstaLock Helmet

<https://chanticleerproducts.squarespace.com/>
<https://youtu.be/CyjRXqkZZsY>

Can Akdere
Mohamed Alwahedi
Omar Asous
John Huang

Evapower

<https://evapower.wixsite.com/website>
<https://youtu.be/ZuYsywIAhFw>

Tanzin Azad
Witold Dziekan
Dev Kanani
Sean Lawrence
John Wendt

BoxAF

<https://ca2816.wixsite.com/boxaf>
<https://youtu.be/Y3rrpzOIbuo>

Colby Andersen
Bryson Baligad
Jan Chmura
Aleksander Zbikowski

Turtle Jets

<https://turtlejetsdishwash.wixsite.com/mysite>
<https://www.youtube.com/watch?v=tlss3idAf7Y>

Pablo Calderon Galaviz
Shiquoi Isaac
Young Jae Ryu

Ball-Bot

<http://Ball-bot.squarespace.com>
<https://youtu.be/IbmHmju5lVk>

Jose Acuna
Mitchell Flautt
Abdul Rayfay
Lithurshanaa Muraleetharan
Donny Steinberg

Podsie

<https://rbs2165.wixsite.com/home>
<https://youtu.be/t-jHMVMEBmE>

Magdy Gad
Annie Lin
Jenna McCune
Robert Sasse
Chen Yang

Autonomous In-space Assembly

<https://lmk2194.wixsite.com/mysite/prototype>
https://youtu.be/sZ6YxcIWu_Y

Rami Hamati
Leon Kim
Henrique Montiero

Humano Detecto

<https://fjs21247.wixsite.com/humanodetecto>
<https://youtu.be/btr-LNHx2HE>

Benjamin Goldsmith
Fernando Jimenez Huerta
Frank Sommers

Free Range Fencing

<https://youtu.be/QmhACmoytBo>

Colm Feeney
Shinya Kondo
Giana Vierheller

FireVzn

<https://cde2119.wixsite.com/firevzn>
<https://youtu.be/oSyBx2tw8gg>

Millen Anand
Connor Evans
Ginny Jeong
Nathalie Limandibhratha

The Carrier Pigeon

<https://codestump.wixsite.com/thepigeon>
https://youtu.be/2oVvUdxu_AY

Shengqiang Chen
Phillip Shnayderman
James Smiley
Kang Yang

Box Extrude

<https://boxxtrude.wixsite.com/home>

<https://youtu.be/b-zJVjRIfmI>

Ridley Eastland-Fruit

Erika Storvick

Conner Warren

Hareem Zain

Smart Spot

<https://kae2146.wixsite.com/smartsport/>

<https://youtu.be/cKeqIYpCRO0>

Kaitlyn Eckart

Josh Guggenheim

Christopher Schoen

Alejo Szybel

Strength Augmenting Exoskeleton Arm

<https://sec2198.wixsite.com/powerarm>

<https://youtu.be/iX4fj0IcOkw>

Sabrina Curtis

Christopher Obiozor

Albert Tai